PCCP

Calculated linear and nonlinear optical absorption spectra of phosphine-ligated gold clusters

Journal:	*Physical Chemistry Chemical Physics*
Manuscript ID	CP-ART-03-2022-001232.R1
Article Type:	Paper
Date Submitted by the Author:	19-Apr-2022
Complete List of Authors:	Day, Paul; US Air Force Research Laboratory, RXAP Pachter, Ruth; Air Force Research Laboratory, Materials & Manufacturing Directorate Nguyen, Kiet ; US Air Force Research Laboratory, RXAP

Calculated linear and nonlinear optical absorption spectra of phosphine-ligated gold clusters

Paul N. Day,[a,b*] Ruth Pachter,[a*] Kiet A. Nguyen[a,b]

[a]Air Force Research Laboratory, Materials and Manufacturing Directorate, Wright-Patterson Air Force Base, OH 45433, USA

[b]UES, Inc. Dayton OH 45432, USA

*authors to whom correspondence should be addressed: paul.day.4.ctr@us.af.mil and ruth.pachter@us.af.mil

Abstract

Although prediction of optical excitations of ligated gold clusters by time-dependent density functional theory (TDDFT) is relatively well-established, limitations still exist, for example in the choice of the exchange-correlation functional. In aiming to improve on the accuracy of the calculated linear absorption, we report a theoretical study on phosphine-ligated gold clusters, specifically $Au_9(PR_3)_8^{3+}$ and $Au_8(PR_3)_7^{2+}$ characterized by highly resolved UV/Vis spectra, using mass-selective electronic absorption photofragmentation spectroscopy (Cirri, A.; Hernández, H. M.; Johnson, C. J. *J. Phys. Chem. A* **2020**, *124*, 1467−1479, and references therein). The optical absorption spectra of the $Au_9(PR_3)_8^{3+}$ and $Au_8(PR_3)_7^{2+}$ clusters were calculated using TDDFT and the many-body GW (G-Green's function, and W-screened Coulomb interaction)-BSE (Bethe Salpeter Equation) method, and compared to the experimental measurements. The evGW-BSE results demonstrated fair agreement with the experimental data, comparable to the TDDFT results, but with less dependence on the reference exchange-correlation functional. Experimentally observed ligand-effects in these materials were reproduced in our calculations as well. Finally, to assess the utility of the materials for nonlinear optical absorption, a theoretical evaluation of two-photon absorption cross-sections is included.

Introduction

Ligand-protected gold clusters, also called aspicules,[1] recently reviewed by Chakraborty and Pradeep,[2] are of interest for catalysis,[3,4] sensing,[5] imaging, bio-tagging,[6] or photovoltaic applications.[7] Interestingly, while the thiol protecting ligands of the gold cluster generally have a "staple" structure[2,8-11] and occasionally a ring,[12] phosphines bond directly to the surface atoms in the gold core.[13-17] The staple-shaped ligands consist of alternating sulfur and gold atoms with the general formula $Au_n(SR)_{n+1}^-$, with n = 0,3, where each sulfur atom bonds to two gold atoms and to the organic group. For example, $Au_{25}(SR)_{18}^-$, has an icosahedral core of 13 gold atoms and 6 "dimer" staples ($Au_2(SR)_3^-$), while $Au_{38}(SR)_{24}$ can be described as a gold core formed by pushing two of the Au_{13} icosahedra together so that they share one triangular face to form Au_{23}, protected by six dimer staple ligands and three monomer ($Au(SR)_2^-$) staple ligands.[11,18-21] In phosphine-ligated gold clusters, however, all the gold atoms are in the core while each phosphorous atom bonds to a gold atom on the core surface as well as to three organic groups. While the phosphine-ligated gold clusters received less attention than those with thiol ligands, they were reported as early as 1969-1970.[22,23] The icosahedral "magic number" Au_{13} gold cluster was investigated,[24,25] and some of the smaller gold clusters, such as Au_{11} and Au_9, could be considered subsets of

Au_{13}.[5,26] Phosphine-ligated clusters with eight or nine gold atoms have been studied both experimentally and theoretically,[14,27-32] but comparison has been limited by the resolution of experimental spectra and by challenges in choosing the theoretical method. Other theoretical studies on small gold clusters have probed the effects of substituting a different atom for a central gold atom[33,34] and of using ligands derived from heterocyclic carbenes in place of phophines.[35-37]

Cirri, et al.[38,39] demonstrated that by using mass-selective electronic absorption photofragmentation spectroscopy, highly-resolved UV/Vis spectra of several such gold clusters were obtained, including $Au_9(PR_3)_8^{3+}$, $Au_8(PR_3)_7^{2+}$, and $Au_8(PR_3)_8^{2+}$, with R = Phenyl (Ph), para-methylphenyl (PhMe), or para-oxymethylphenyl (PhOMe). With some similarity to HPLC, this method uses mass spectrometry to separate a mixture and obtain spectra of the individual components. Action spectroscopy[40] techniques were used to amplify the signal to a feasible level. The highly resolved optical properties for this class of clusters are appropriate for assessment of the prediction accuracy by first principles calculations, as well as in elucidating the specific transitions in the resulting spectra.

Time-dependent density functional theory (TDDFT) is well-established for calculation of the optical excitations of molecules and clusters, but its dependence on the choice of exchange-

correlation (X-C) functional[41] still limits its reliability and applicability. With the goal of improving the accuracy of calculated linear absorption spectra, we evaluate the many-body GW (G-Green's function, which describes the particle in an interacting system based on density functional theory (DFT), and W-screened Coulomb interaction)-BSE (Bethe Salpeter Equation)[42,43] method. The GW method, an approximate solution of the Hedin equations,[42,44] improves on DFT in the calculation of the electronic energy eigenvalues, where GW quasiparticle energies are used instead of the Kohn-Sham energies, and with the BSE the excitons are calculated. This approach enabled the study of excitonic effects for two-dimensional solid systems,[45-48] and was extended to molecular systems as well.[44,49,50] While fully self-consistent GW-BSE calculations are computationally prohibitive in this case, the GW solution without iterations to self-consistency (G_0W_0) or the eigenvalue self-consistent method evGW[51-53] can be applied, having the advantage of lesser dependence on the XC functional.[53] In the evGW method, the corrected eigenvalues are used to recalculate the polarizability and the Green's function, which are then used to calculate updated quasiparticle energies, and the process is iterated to self-consistency. The evGW method avoids the significant computational cost of a fully self-consistent GW, and it was shown previously that not updating the eigenfunctions has a very limited impact on the final

result.[53] A disadvantage of the GW-BSE approach is that analytic gradients are not available to calculate forces. In some cases, this problem has been circumvented by using DFT forces in combination with BSE vertical excitation energies.[54]

In this work, we calculated the one-photon and two-photon absorption spectra (OPA, TPA) for $Au_9(PR_3)_8^{3+}$ and $Au_8(PR_3)_7^{2+}$ (R = Ph, PhMe, and PhOMe) using TDDFT and GW-BSE, comparing to the measured spectra. Two structural forms[14,29,32,55,56] have been identified for the $Au_9(PR_3)_8^{3+}$ cluster, the so-called "butterfly" structure with D_2 symmetry, previously studied theoretically,[30] and the "crown" structure with C_4 symmetry, which was recently investigated as well.[31] A recent study[57] included two versions of the butterfly structure, the first of which, labeled $D_2(1)$, is close to D_{2h} symmetry with the two 5-atom gold planes nearly perpendicular, while the second, labeled $D_2(2)$, is twisted significantly. Here we focus on the D_2 structure, but include calculated results on the C_4 structure as well.

While Fagan, et al.[57] reported good agreement with experiment using scaled TD-GRAC on $Au_8(PPh_3)_7^{2+}$, they did not find good agreement for $Au_9(PR_3)_8^{3+}$ using either their scaled or unscaled TD-GRAC[58] spectra. They applied linear scaling of the TD-GRAC spectra to mitigate the known problem[8,11,59,60] of underestimation of excitation energies when using GGA functionals

with TDDFT. We found that the evGW-BSE results are in good agreement with experiment with both reference functionals, and with less dependence on the reference functional than when using TDDFT. We chose the hybrid PBE0 functional due to its demonstrated predictive capability of TDDFT excitation energies, as well as the range-separated CAMB3LYP functional, shown to be appropriate for excited-states with large charge transfer. In order to verify the decreased dependence on the reference functional, two more functionals, B3LYP and PBE, were also tested. Examination of the origin of the excitations showed that the super-atom theory is useful even as the increased deviations from spherical symmetry increase the distortion of the super-atom orbitals from the shape of the classic atomic orbitals.

However, in comparing to measured OPA spectra, we emphasize that some caveats must be considered in the calculated vertical excitation energies.[53] The vertical absorption energy is often a reasonable approximation for the vibronic excitation energy, but the actual absorption can range from as low as the 0-0 energy to higher than the vertical excitation energy, dependent on the Franck-Condon factors for vibrational overlap. In addition, the theoretical calculations frequently do not properly account for environmental factors such as solvent, difficulties which can be

mitigated by comparing to theoretical best estimates[53] or through corrections for solvation and vibrational factors.[61]

We also evaluated the utility of these clusters for two-photon absorption (TPA), as materials with large TPA cross-sections are of interest for applications such as microfabrication, optical memory, and photodynamic therapy, and thiolated gold clusters have been found to have large TPA cross-sections.[62,63] Our results indicate relatively small TPA cross-sections, particularly for $Au_8(PR_3)_7^{2+}$, but larger values for $Au_9(PR_3)_8^{3+}$, which could motivate experimental exploration.

Computational Methods

The Def2-TZVP basis set and its associated effective core potential, which was designed to include relativistic effects, was used for gold atoms, while the Def2-SVP basis was used for all other atoms.[64] The geometry was optimized with the Gaussian 16 program[65] using the PBE0 functional[66] and the D3 dispersion correction,[67] and each geometry was confirmed to be a minimum with a vibrational frequency calculation. Turbomole[49,68-74] was used to carry out the TDDFT and GW-BSE calculations.[44,49,52] Resolution of Identity (RI) was used in both the DFT and GW steps. The TDDFT and GW steps were carried out with both the PBE0[66] and CAMB3LYP[75] X-C functionals. To further assess the dependence on the X-C functional,

calculations were carried out with the GGA functional PBE[76] and with the hybrid functional B3LYP.[77,78] The RI GW method in Turbomole constructs the self-energy on the imaginary axis using numerical integration, and the obtained result is then analytically continued to the real axis using Pade approximates. The RI GW was carried out with all occupied orbitals and one virtual orbital, and the orbitals were shifted by the HOMO-LUMO gap. The number of Pade approximates and the number of imaginary frequency integration points were both kept at the Turbomole default value of 128.

The spectra were obtained from the calculated excitation energies and oscillator strengths using normalized Gaussian lineshape functions:

$$\varepsilon(\tilde{\nu}) = \frac{2\sqrt{\ln 2}}{4.32 \times 10^{-9}\sqrt{\pi}} \sum_i \frac{f_i}{\tilde{\nu}_i^{FWHM}} \exp\left[\frac{-4\ln 2}{\left(\tilde{\nu}_i^{FWHM}\right)^2}(\tilde{\nu} - \tilde{\nu}_i)^2\right], \quad (1)$$

where $\varepsilon(\tilde{\nu})$ is the extinction coefficient at the transition frequency $\tilde{\nu}$, while $\tilde{\nu}_i$ and f_i are the transition frequency (in cm^{-1}) and oscillator strength, respectively, corresponding to the excited state *i*, and $\tilde{\nu}_i^{FWHM}$ is the full-width at half-maximum of the Gaussian function used to fit the state *i*.

The TPA cross-section was calculated as we described previously,[79-81] given by

$$\delta_{f0}(2E_\lambda) = \frac{8\pi^4}{(ch)^2} E_\lambda^2 g(2E_\lambda) |S_{f0}|^2 \quad (2)$$

where E_λ is the photon energy, *c* is the speed of light, *h* is Plank's constant, $g(2E_\lambda)$ is the linewidth function which might be a Gaussian or a Lorentzian, and $|S_{f0}|^2$ is the two-photon probability

corresponding to a transition from the ground-state (*0*) to the final state (*f*), which can be described by a sum-over-states (SOS) expression,

$$|S_{f0}|^2 = \left|\sum_j^N \frac{2\mu_{j0}\mu_{fj}}{E_j - E_\lambda + i\Gamma_j}\right|^2 \quad (3)$$

where μ denotes a transition dipole moment, E_j is the energy of state *j*, and Γ_j is the decay constant for state *j*, a damping factor. We used a Gaussian linewidth function, given by,

$$g(2E_\lambda) = \left(\frac{4h^2 ln2}{\pi E_{fwhm}^2}\right)^{1/2} exp\left[\frac{-4ln2}{E_{fwhm}^2}(2E_\lambda - E_f)^2\right] \quad (4)$$

The maximum of the linewidth function *g* occurs when $E_\lambda = E_f/2$, resulting in a resonant condition if $E_j = E_f/2$. If the two-photon probability is evaluated using the SOS expression, Eq. (3), the damping factor, Γ_j, mitigates unrealistic resonance effects. The two-photon probability can also be obtained analytically as the residue of the quadratic response function, which is more computationally efficient than calculating the full matrix of transition dipole moments as would be needed to carry out the complete SOS. We used the more efficient analytical method to obtain the two-photon probability, as implemented in Turbomole.[82] For the two-photon linewidth, E_{fwhm}, we used a value of 0.1 eV. Since the maximum of the linewidth function is inversely proportional to the linewidth, the calculated TPA cross-section has this dependence as well. To avoid the resonance, the TPA cross-sections were considered for $E_f < 2E_j$ for all excited states *j*.

Results and Discussion

Structures.

The structure for $Au_8(PR_3)_7^{2+}$ with R = Ph was obtained by starting with the crystal structure coordinates of van der Veldon, et al.[83] (obtained from the Cambridge Crystallographic Data

Centre), adding hydrogen atoms, and optimizing with PBE0-D3. Structures for R = PhMe and with R = PhOMe were obtained by substituting the ligands in the structure and re-optimizing with PBE0-D3. For $Au_9(PR_3)_8^{3+}$ with R = Ph, we started with the crystal structure of Wen et al.[27] and obtained an optimized geometry with approximate D_2 symmetry using PBE0-D3. We obtained a C_4 or "crown" geometry with R = Ph from Yamazoe, et al.[32] and re-optimized it using PBE0-D3. The structures for $Au_9(PR_3)_8^{3+}$ with R = PhMe and with R = PhOMe were obtained by substituting the ligands in these structures and re-optimizing with PBE0-D3. Figure 1 shows the gold core structures for the two $Au_9(PR_3)_8^{3+}$ isomers, D_2 and C_4, and for $Au_8(PR_3)_7^{2+}$. The $Au_8(PR_3)_7^{2+}$ cluster is similar to the D_2 isomer of $Au_9(PR_3)_8^{3+}$, but with one surface gold atom and its associated PR_3 ligand removed. The core structures are shown in Figure 1 and full structures with ligands are shown in Figure S1.

Table 1 lists the geometrical parameters for our optimized structures of $Au_8(PR_3)_7^{2+}$, including previously reported values. The average Au-Au bond length is smallest for the crystal structure, but our PBE0-D3 geometry with R=Ph is larger by only 0.02 Å. The average value found previously using BP86[57] is 0.05 Å larger than the PBE0-D3 value. The value found previously[84] using the dispersion-corrected PBE-D3 functional is nearly identical to the PBE0-D3 value we

report here, indicating that the larger value in the BP86 geometry is mostly due to the exclusion of dispersion effects in the geometry optimization. The 16 Au-Au bonds are grouped into two categories: the first including the seven radial bonds (those between the center Au atom and the surface gold atoms) and the second having the nine surface bonds. The radial bonds are shorter than the surface bonds by an average of 0.18 Å using PBE0-D3 and by similar amounts in the other results. The average Au-P bond length calculated using PBE0-D3 is also slightly longer than in the crystal structure and moderately smaller than in the BP86 structure. The effects of the ligands R=PhMe and R=PhOMe on the core bond lengths are very small.

A comparison of the experimental and calculated bond lengths for the Au_9 cluster are listed in Table 2. The crystal structure geometry for the D_2 geometry with R = Ph is from Wen et al.,[27] while the only crystal structure available for the C_4 geometry is with R = PhOMe.[14] For both the D_2 and C_4 structures, the crystal structure has a more compact core than was obtained through DFT optimization. For the D_2 geometry with R = Ph, the previously reported BP86,[57] B3LYP,[32] and PBE-D3[84] optimized structures have average Au-Au bond lengths larger by 0.10, 0.15, and 0.04 Å, respectively, and for our PBE0-D3 optimized structure larger by 0.03 Å, demonstrating the importance of including a London dispersion correction in the geometry optimization.

The C_4 isomer of $Au_9(PR_3)_8^{3+}$ with R = Ph was studied by Madridejos, et al.,[31] where the geometry was optimized by a tight-binding method. Using PBE0-D3 and R = Ph, we found the ground-state of the C_4 structure to be about the same energy as the D_2 structure, specifically 0.01 eV (0.23 Kcal/mole) higher in energy than the ground-state for the D_2 structure. Like the D_2 structure, the C_4 structure has eight radial Au bonds, but unlike the former, which has 12 surface bonds, it has only eight surface bonds. Our PBE0-D3 calculated average Au-Au bond length is smaller for the C_4 structure than for the D_2 structure. As can be seen in Table 2, their reported[31] DFT2B-D3 optimized structure is surprisingly compact with an average Au-Au bond length 0.10 Å smaller than our PBE0-D3 result. Consistent with previous results, the BP86 and B3LYP values are larger by 0.05 and 0.11 Å, respectively.

Optical absorption spectra: $Au_8(PR_3)_7^{2+}$. Comparison of calculated linear absorption spectra for the $Au_8(PR_3)_7^{2+}$ cluster with the high-resolution absorption spectra (denoted as H.R. henceforth) reported by Cirri, et al.[39] is reported in Figure 2, Table 3, and Figures S2-S4 in the Supplementary Material. Overall, as expected, results based on the CAMB3LYP functional are blue-shifted

Table 1. Comparison of the crystal structure[83] and calculated average, minimum, and maximum Au-Au and Au-P bond-lengths (Å) for $Au_8(PR_3)_7^{2+}$.

	R=Ph crystal[83]	R=Ph BP86[57]	R=Ph PBE-D3[84]	R=Ph PBE0-D3	R=PhMe PBE0-D3	R=PhOMe PBE0-D3
ave Au-Au	2.78	2.85	2.81	2.80	2.80	2.81
min Au-Au	2.63	2.69	2.65	2.62	2.62	2.62
max Au-Au	2.94	3.03	2.96	3.05	3.09	3.08
Au-radial	2.68	2.75		2.70	2.70	2.70
Au-surface	2.85	2.93		2.88	2.88	2.89
ave Au-P	2.30	2.36	2.33	2.32	2.32	2.32
min Au-P	2.24	2.34	2.31	2.30	2.30	2.30
max Au-P	2.36	2.37	2.34	2.34	2.33	2.34

compared to those calculated with PBE0, but this functional dependence is decreased significantly in the evGW-BSE calculations. The first OPA peaks calculated using TDDFT for the cluster with the R = Ph, PhMe, and PhOMe ligands, were blue-shifted by 0.20, 0.21, and 0.21 eV, respectively, when CAMB3LYP was used vs. PBE0, while the blue-shift was only 0.06, 0.06, and 0.05 eV in the evGW-BSE calculations. For R=Ph, the functional dependence was also evaluated using B3LYP and PBE; for B3LYP, the first OPA peak was red-shifted 0.09 eV compared to the PBE0 result, but this difference was reduced to 0.02 eV with evGW-BSE, while TD-PBE tends to underestimate excitation energies and the first excitation is 0.33 eV lower than the PBE0 result, reduced to 0.07 eV when evGW-BSE is used. The decrease in the dependence on the X-C functional was also observed for the higher-energy excitations.

As seen in Figure 2 and Table 3, evGW-BSE:PBE0 performs well in predicting the first transition energy for these systems, overestimating the energy by just 0.01, 0.08, and 0.05 eV. We evaluated the agreement of the calculated spectra with experiment using the mean-unsigned-error (MUE) in the transition energy relative to measurement for the first six features. Note that some of the calculated intensities do not agree well with the measured values, and this is known to be

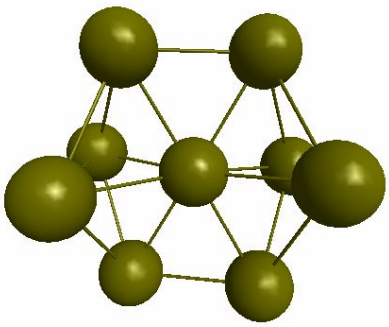

a)

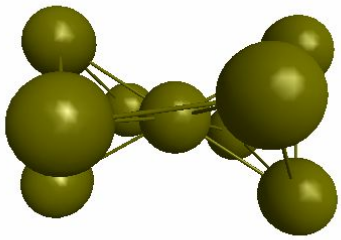

b)

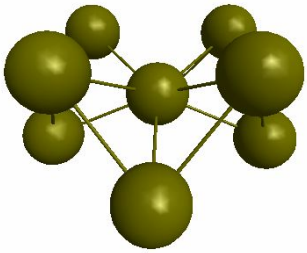

c)

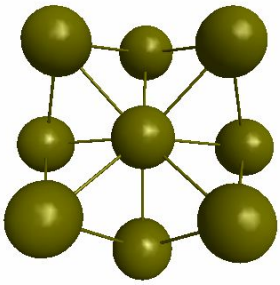

d)

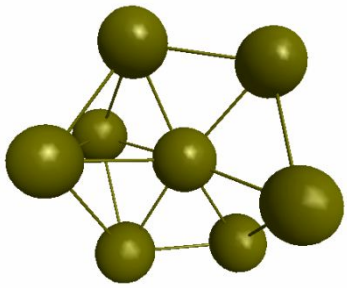

e)

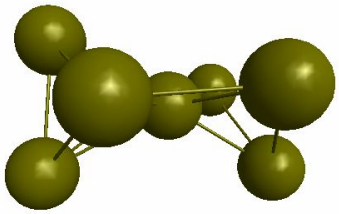

f)

Figure 1. The Au cores of the clusters studied. a) (side-view) and b) (top-view) show the D_2 or "butterfly" structure from $Au_9(PR_3)_8^{3+}$ (R = Ph) optimized using the PBE0-D3 X-C functional, while c) and d) show the C_4 or "crown" structure. In e) and f) the core from $Au_8(PR_3)_7^{2+}$ is shown.

Table 2. Comparison of the crystal structure[14,27] and calculated average, minimum, and maximum Au-Au and Au-P bond-lengths (Å) for D_2 (butterfly) and C_4 (crown) $Au_9(PR_3)_8^{3+}$.

	R=Ph D_2 crystal[27]	R=Ph D_2(1) BP86[57]	R=Ph D_2(2) BP86[57]	R=Ph D_2 PBE-D3[84]	R=Ph D_2 B3LYP[32]	R=Ph D_2 PBE0-D3
ave Au-Au	2.78	2.88	2.89	2.82	2.93	2.81
min Au-Au	2.67	2.82	2.77	2.73	2.81	2.71
max Au-Au	2.88	2.97	3.05	2.92	3.03	2.91
Au-radial	2.69	2.79	2.80		2.84	2.72
Au-surface	2.83	2.93	2.94		2.99	2.87
ave Au-P	2.28	2.37	2.38	2.33	2.42	2.32
min Au-P	2.27	2.35	2.35	2.32	2.40	2.30
max Au-P	2.29	2.39	2.40	2.35	2.45	2.33

	R=PhOMe C_4 crystal[14]		R=Ph C_4 BP86[57]	R=Ph C_4 DFT2B-D3[31]	R=Ph C_4 B3LYP[32]	R=Ph C_4 PBE0-D3
ave Au-Au	2.74		2.82	2.67	2.88	2.77
min Au-Au	2.65		2.78		2.80	2.70
max Au-Au	2.84		2.88		2.96	2.84
Au-radial	2.66		2.78	2.63	2.81	2.70
Au-surface	2.82		2.87	2.71	2.96	2.84
ave Au-P	2.29		2.36	2.31	2.41	2.31
min Au-P	2.28		2.36		2.41	2.31
max Au-P	2.30		2.36		2.41	2.31

	R=PhMe D_2 PBE0-D3	R=PhOMe D_2 PBE0-D3	R=PhMe C_4 PBE0-D3	R=PhOMe C_4 PBE0-D3
ave Au-Au	2.81	2.81	2.77	2.77
min Au-Au	2.70	2.71	2.68	2.69
max Au-Au	2.91	2.91	2.89	2.87
Au-radial	2.72	2.72	2.69	2.70
Au-surface	2.86	2.86	2.85	2.85
ave Au-P	2.32	2.32	2.31	2.31
min Au-P	2.30	2.31	2.30	2.31
max Au-P	2.33	2.33	2.32	2.32

a challenging problem.[85] The calculated MUE is lowest using TD-PBE0, evGW-BSE:PBE0, and evGW-BSE:CAMB3LYP. With CAMB3LYP, the G_0W_0-BSE spectrum is quite close to the evGW-BSE spectrum, and thus also has a low MUE. The TD-CAMB3LYP method usually overestimates the excitation energies, while G_0W_0-BSE:PBE0 tends to underestimate these values. For $Au_8(PR_3)_7^{2+}$ (R = Ph), the first peak in the measured spectrum for this cluster is at 2.07 eV, and the evGW-BSE:PBE0 result is in excellent agreement with a difference of only 0.01 eV. The CAMB3LYP evGW-BSE and G_0W_0-BSE calculations overestimate the measured value by just 0.07 and 0.09 eV, respectively, while TD-PBE0 and TD-CAMB3LYP overestimate the value by 0.12 and 0.32 eV, respectively, and PBE0:G_0W_0-BSE underestimates it by 0.16 eV. The evGW-BSE:PBE0 method is also in good agreement with experiment for the other two ligands, overestimating the transition energy for the first peak by just 0.08 eV and 0.05 eV for R = PhMe and PhOMe, respectively. The evGW-BSE:PBE0 results have good agreement with the transition energies for the higher energy peaks in the spectrum, as the MUE values are 0.08, 0.08, and 0.07 eV for the three ligands, respectively. Note that for R = PhOMe, the shoulder at 2.78 eV is considered a feature in the measured spectrum.

In compiling the features in the measured H.R. spectrum, we focused on the peaks in the spectrum, but a recent publication[57] resolved the original measured H.R. spectrum[39] for $Au_8(PR_3)_7^{2+}$, R = Ph, using Voigt lineshape functions, and instead of just six features with transition energies below 3.5 eV, they reported eleven features, with the peaks at 2.42, 2.75, and 3.07 eV each split into two features and the peak at 3.39 eV resolved into three features. As the authors noted,[57] their analysis is not necessarily a complete or unique resolution of the absorption spectrum. We have carried out an alternative analysis of our computed results by comparing the

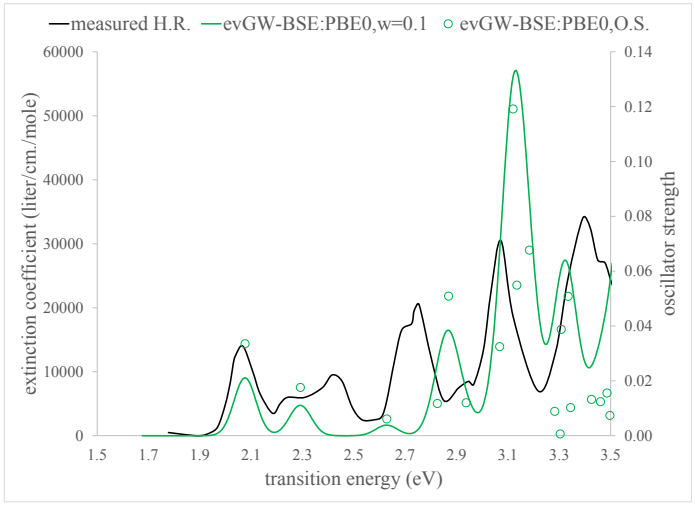

a)

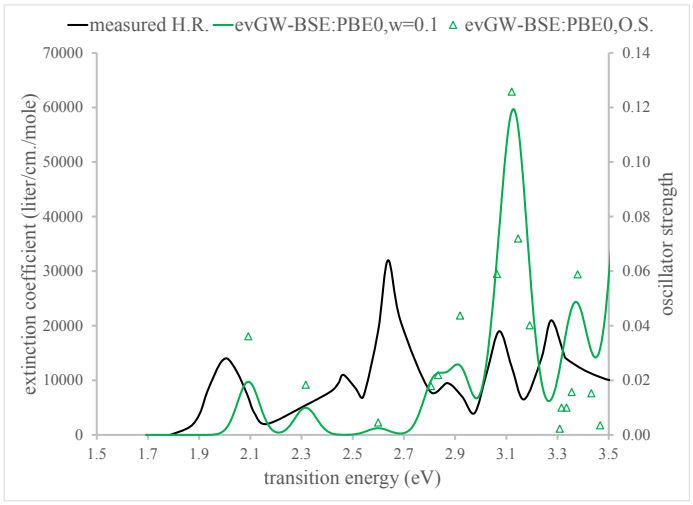

b)

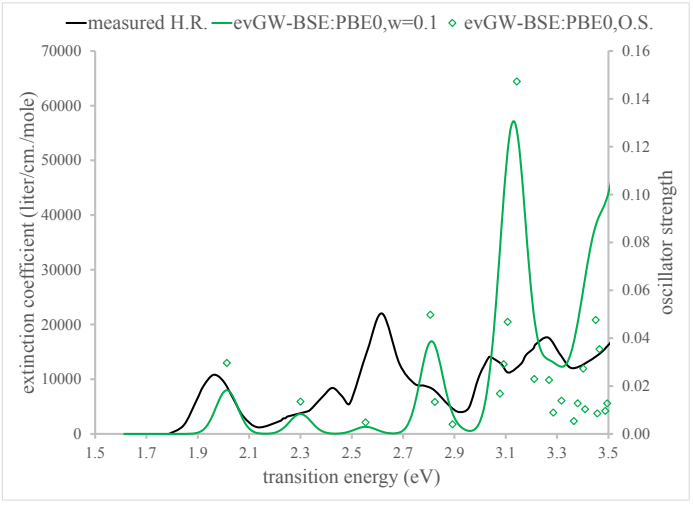

c)

Figure 2. Measured H.R. and calculated evGW-BSE:PBE0 linear absorption spectra, including

oscillator strengths (O.S.), for $Au_8(PR_3)_7^{2+}$. a) R = Ph, b) PhMe, and c) PhOMe.

Table 3. OPA features (in eV) for $Au_8(PR_3)_7^{2+}$, R = Ph, PhMe, and PhOMe. All features are peaks in the spectrum with the exception of the measured feature at 2.78 eV for R = PhOMe, which is a shoulder. The calculated results used a geometry optimized with PBE0-D3, and the calculated oscillator strengths were fitted with a Gaussian linewidth function with width = 0.1 eV. The measured results are the mass-selective UV/Vis maxima taken from spectra of Cirri, et al.[39] The mean unsigned error (MUE) is the average of the absolute error of the first six features relative to the measured value. The labels evGW and G_0W_0 refer to the GW-BSE calculations with the eigenvalue-iterated GW and non-iterated GW, respectively, while CAM refers to the CAMB3LYP functional.

R = Ph									**MUE**
measured	2.07	2.42	2.75	2.95	3.07	3.39	3.67	4.09	
TD-PBE0	2.19	2.41	2.70	2.95	3.23	3.47	3.72	3.97	**0.07**
G_0W_0:PBE0	1.90	2.12	2.45	2.69	2.96	3.15	3.42	3.55	**0.23**
evGW:PBE0	2.08	2.29	2.63	2.87	3.13	3.32	3.59	3.73	**0.08**
TD-CAM	2.39	2.67	3.02	3.31	3.57	3.70	3.77	3.94	**0.33**
G_0W_0:CAM	2.16	2.43	2.80	3.03	3.37	3.52	3.68	3.96	**0.11**
evGW:CAM	2.13	2.40	2.77	3.00	3.34	3.49	3.65	3.93	**0.09**
TD-B3LYP	2.10	2.32	2.61	2.84	3.16	3.38	3.59	3.75	**0.08**
evGW:B3LYP	2.06	2.28	2.62	2.86	3.11	3.29	3.56		**0.08**
TD-PBE	1.86	1.98	*2.26*	2.50	2.67	2.83	3.03		**0.43**
evGW:PBE	2.01	2.13	2.51	2.78	2.91	3.20			**0.19**
R = PhMe									**MUE**
measured	2.01	2.46	2.64	2.87	3.07	3.28	3.87	4.11	
TD-PBE0	2.19	2.42	2.66	2.93	3.21	3.50	3.69	3.96	**0.11**
G_0W_0:PBE0	1.92	2.15	2.43	2.74	2.96	3.20	3.41	3.55	**0.16**
evGW:PBE0	2.09	2.32	2.60	2.91	3.13	3.37	3.58	3.72	**0.08**
TD-CAM	2.40	2.69	2.95	3.26	3.54	3.73	4.01	4.22	**0.37**
G_0W_0:CAM	2.18	2.46	2.74	2.97	3.14	3.28	3.38	3.53	**0.07**
evGW:CAM	2.15	2.43	2.71	2.94	3.11	3.25	3.35	3.50	**0.06**
R = PhOMe									**MUE**
measured	1.96	2.43	2.62	2.78	3.04	3.27	3.57	3.81	
TD-PBE0	2.13	2.43	2.64	2.91	3.25	3.55	3.77		**0.09**
G_0W_0:PBE0	1.85	2.13	2.39	2.64	2.96	3.49			**0.16**
evGW:PBE0	2.01	2.30	2.55	2.81	3.13	3.66			**0.07**
TD-CAM	2.34	2.70	2.93	3.27	3.62	3.76	4.00	4.21	**0.37**
G_0W_0:CAM	2.10	2.45	2.72	2.98	3.39	3.61	3.82	4.13	**0.14**
evGW:CAM	2.07	2.42	2.69	2.95	3.36	3.58	3.79	4.10	**0.11**

first eleven excited-states in each of our calculations to these resolved features, and have reported the results in Table S1. While the analysis from Table 3 did not distinguish between electronic and vibrational line-broadening, the analysis in Table S1 assumes that these eleven features are all electronic excited-states. Using this analysis, the evGW-BSE:PBE0 calculation again yields low MUE, as does evGW-BSE:B3LYP. The TD-B3LYP MUE is slightly lower than that using TD-PBE0, while the error in the evGW-BSE:CAMB3LYP calculation is not as low. Otherwise, this analysis yields similar conclusions about the methods as from the analysis in Table 3, particularly the reduced dependence on the X-C functional when evGW-BSE is used. Table S1 also lists the primary orbital transition for each excited-state, which will be discussed below.

We described two methods for evaluating the error in comparison to experiment, specifically by direct comparison of the calculated and measured peaks (Table 3), and by comparing the calculated excited-state energies to the resolved peaks of Fagan, et al.[57] (Table S1). The results yield a relatively low MUE over the energy range 2.0 – 3.5 eV for both TD-PBE0 and evGW-BSE:PBE0. In examining the low-energy part of the spectrum (2.0 – 2.5 eV), we note that each of

these theoretical methods yields two excited-states in this range and thus two features, while the resolved experimental spectrum of Fagan, et al.[57] has three peaks in this energy range. This seems to indicate that the two resolved peaks at 2.26 eV and 2.42 eV are from vibrational splitting of the second excited-state. The first excited-state calculated using evGW-BSE:PBE0 is just 0.02 eV higher in energy than the first peak in the resolved experimental spectrum, and the second calculated peak is just 0.03 eV higher than the resolved feature at 2.26 eV. Since the next calculated excited-state is at 2.63 eV, we suggest that the resolved feature at 2.42 eV is also from the second electronic excited-state but with a larger vibrational energy. Note that although the analysis in Table S1 simply lists the excited-state energies without consideration of the calculated intensity, the analysis in Table 3 is derived from the Gaussian-fit of the calculated oscillator strengths as shown in Figures 2 and S2 - S4.

Optical absorption spectra: $Au_9(PR_3)_8^{3+}$. Previous experimental and theoretical studies indicated that the C_4, or crown geometry, is favored in solution,[31,32] while the D_2, or butterfly, geometry is found in the solid phase.[27] Our geometry optimizations using PBE0-D3 on $Au_9(PR_3)_8^{3+}$ indicate that the two isomers are very close in energy, with the D_2 geometry lower in energy by 0.01 eV when R = Ph, and with the C_4 structure lower in energy by 0.11 eV and 0.01 eV for R = PhMe and

PhOMe, respectively. In a previous theoretical study[32] using B3LYP, the C_4 structure was reported to be lower in energy by 0.21 eV when R = Ph. This discrepancy could be due to our inclusion of the D3 correction for dispersion, which was not included in Ref.[32]. The difference of 0.11 eV for the R = PhMe cluster may seem to favor the C_4 isomer at low temperature, but due to the limited accuracy of DFT, we consider the possibility that both isomers are present. First, we discuss the choice of the structure for consideration, as based on a comparison of experimental and theoretical absorption spectra for $Au_9(PR_3)_8^{3+}$ with R = Ph, in DCM and methanol (listed in Table S2). The two measured spectra in methanol[31,39] agree well for the features at 2.80 eV, 3.26 eV, and 3.53 eV, but the Ref.[31] measurement does not show the features at 1.97 eV, 2.42 eV, and 3.00 eV. The theoretical calculations indicate that the low-energy absorption near 2.0 eV is from the D_2 structure, and we suggest that the Ref.[31] measurements are indeed on the C_4 isomer, as is that of Ref.[29] in acetonitrile. The Ref.[39] measurements have the peak near 2.0 eV, indicating the presence of the D_2 structure, although these spectra could also result from a combination of the D_2 and C_4 clusters. Our TD-PBE0 calculation on the C_4 geometry is in good agreement with the SO-TDDFT results,[31] having peaks near 2.9 eV and 3.4 eV, although solvent effects or spin-orbit coupling (SOC) were not included in our calculations. The primary effect of including SOC is the addition

of the feature at 3.15 eV, which interestingly is difficult to observe in their measured spectrum.[31] The TD-PBE0 feature we report at 2.35 eV is of negligible intensity, and the small intensity peak at 2.74 eV could be missed using a different linewidth function. We note that solvent effects were found to be minimal,[31] while inclusion of SOC will affect the absorption tail that is not considered here. To consider the possibility of a mixture of the two structures in the measured spectrum,[39] we also summarized results for an average of the calculated spectra from the two isomers. We found a reduction in the MUE relative to experiment for the results at the TD-PBE0 level and for evGW-BSE with both functionals.

Absorption spectra for $Au_9(PR_3)_8^{3+}$ (R = Ph, PhMe, and PhOMe) are shown in Figure 3 and Figures S5 – S7, and the absorption features are tabulated in Table 4. While the calculated first OPA peaks for the three D_2 clusters were blue-shifted by 0.18, 0.19, and 0.21 eV in the TDDFT calculations using the CAMB3LYP functional (rather than PBE0), the blue-shift was only 0.06, 0.05, and 0.04 eV in the evGW-BSE calculations, demonstrating yet again that the evGW-BSE results show less dependence on the reference X-C functional than TDDFT. This was also observed for the higher-energy excitations. This is an important outcome, as one can avoid the extensive benchmarking of TDDFT with a range of functionals.

The first peak in the high-resolution measured spectrum for $Au_9(PR_3)_8^{3+}$ with R = Ph is at 2.04 eV. Our PBE0 TDDFT, G_0W_0-BSE, and evGW-BSE spectra calculated on the D_2 geometry result in lower energies by 0.11 eV, 0.37 eV, and 0.22 eV, respectively. The CAMB3LYP TDDFT result is at a higher energy by 0.08 eV, while the corresponding G_0W_0-BSE, and evGW-BSE calculated spectra show a lower energy than experiment by 0.13 eV and 0.16 eV,

a)

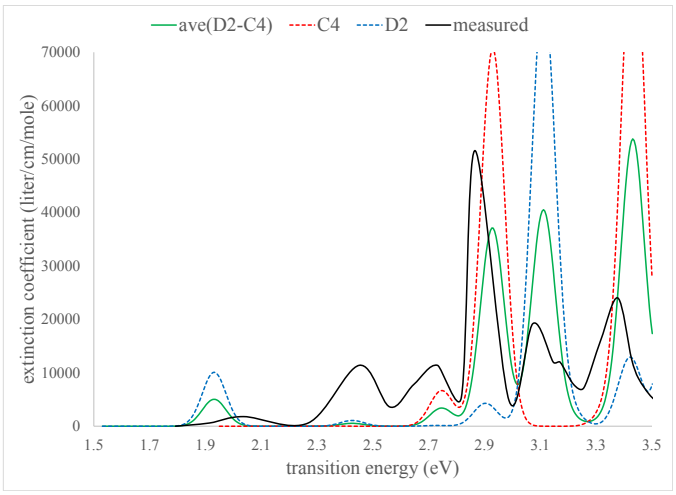

b)

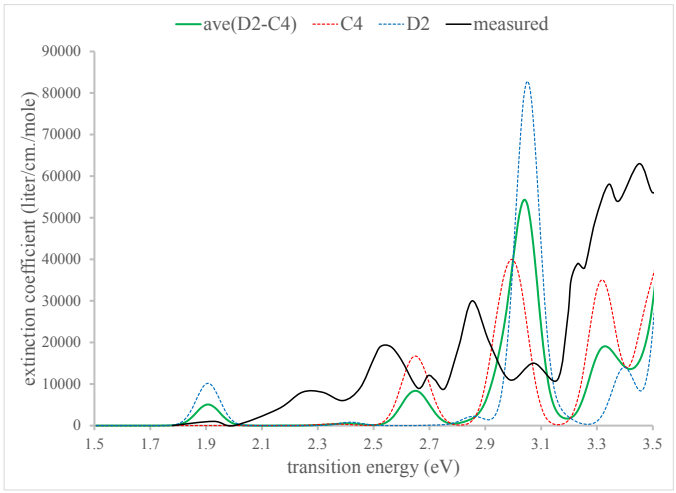

c)

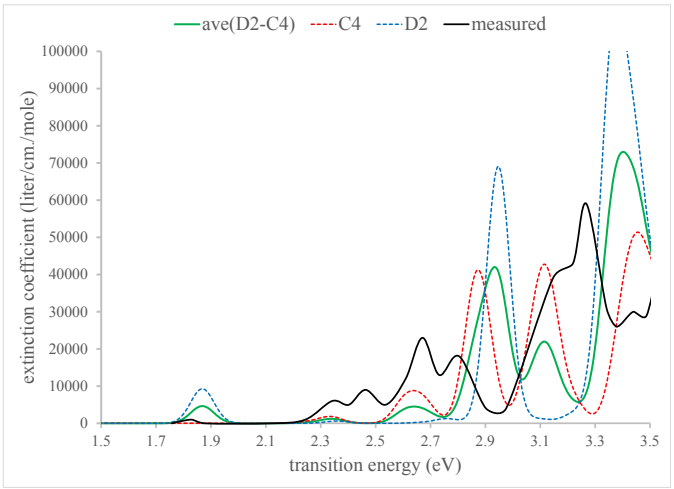

Figure 3. Calculated linear absorption spectra for $Au_9(PR_3)_8^{3+}$ using TDDFT with PBE0, averaging the spectra (solid green line) from the D_2 (dashed blue line) and C_4 (dashed red line) geometries, with comparison to the measured H.R. spectra . a) R = Ph, b) PhMe, and c) PhOMe.

Table 4. OPA peaks (in eV) for $Au_9(PR_3)_8^{3+}$, R = Ph, PhMe, and PhOMe. The calculated results used the D_2 and C_4 geometries optimized with PBE0-D3, and the calculated oscillator strengths were fitted with a Gaussian linewidth function with width = 0.1 eV. The measured results are the high-resolution mass-selective UV/Vis maxima taken from spectra of Cirri, et al.[39] The mean unsigned error (MUE) is the average of the absolute error of the first five peaks relative to the measured value.

R=Ph								**MUE**
measured	2.04	2.45	2.73	2.87	3.07	3.38	3.60	
D_2 isomer								
TD-PBE0	1.93	2.43	2.90	3.11	3.42	3.61	3.71	**0.18**
G_0W_0:PBE0	1.66	2.15	2.63	2.84	3.17		3.38	**0.18**
evGW:PBE0	1.82	2.31	2.79	3.00	3.33		3.54	**0.16**
TD-CAM	2.12	2.74	3.23	3.58	3.84	4.13	4.31	**0.47**
G_0W_0:CAM	1.90	2.50	2.98	3.27	3.57	3.77	3.98	**0.27**
evGW:CAM	1.88	2.47	2.95	3.25	3.54	3.75	3.95	**0.25**
C_4 isomer								
TD-PBE0	2.35	2.75	2.93	3.44	3.63	3.80	3.93	
evGW:PBE0	2.27	2.65	2.83	3.34	3.81			
evGW:CAM	2.30	2.68	2.89	3.41	3.64	3.77	3.98	
(D_2,C_4) average								
TD-PBE0	1.93	2.43	2.75	2.93	3.11	3.43	3.61	**0.05**
evGW:PBE0	1.82	2.30	2.65	2.83	3.00	3.34	3.54	**0.11**
evGW:CAM	1.88	2.47	2.68	2.90	3.25	3.42	3.64	**0.09**
R=PhCH$_3$								
measured	1.93	2.32	2.56	2.70	2.85	3.45	3.56	
					3.07	*3.23*	*3.34*	
D_2 isomer								
TD-PBE0	1.91	2.21	2.42	2.86	3.05	3.40	3.62	**0.13**
G_0W_0:PBE0	1.65	1.99	2.15	2.60	2.80	3.16	3.33	**0.23**
evGW:PBE0	1.80	2.14	2.30	2.75	2.95	3.31	3.48	**0.14**
TD-CAM	2.09	2.44	2.73	3.19	3.53	3.81	4.10	**0.33**
G_0W_0:CAM	1.89	2.27	2.51	2.95	3.22	3.56	3.75	**0.15**
evGW:CAM	1.86	2.23	2.47	2.92	3.19	3.52	3.72	**0.16**
C_4 isomer								
TD-PBE0	2.36	2.65	3.00	3.32	3.59			
(D_2,C_4) average								
TD-PBE0	1.91	2.41	2.65	3.04	3.33	3.61	3.85	**0.08**

R=PhOCH3								
measured	1.83	2.34 *2.46*	2.67	2.80	3.27	3.44	3.57	
D_2 isomer								
TD-PBE0	1.87	2.36	2.76	2.95	3.38	3.71		**0.08**
G_0W_0:PBE0	1.63	2.12	2.52	2.71	3.12	3.29	3.43	**0.16**
evGW:PBE0	1.79	2.27	2.62	2.87	3.27	3.45	3.58	**0.05**
TD-CAM	2.07	2.71	3.15	3.46	3.78	4.13	4.35	**0.43**
G_0W_0:CAM	1.86	2.46	2.90	3.10	3.50	3.67	3.98	**0.16**
evGW:CAM	1.83	2.43	2.86	3.06	3.46	3.64	3.94	**0.14**
C_4 isomer								
TD-PBE0		2.33	2.64	2.87	3.11	3.45	3.70	
(D_2,C_4) average								
TD-PBE0	1.87	2.34	2.64	2.93	3.11	3.40	3.70	**0.07**

respectively. For comparison to the intense peak in the experimental data at 2.87 eV, the peak at 2.84 eV in the G_0W_0-BSE:PBE0 calculation appears to be in good agreement; however, this is likely a cancellation of errors as the G_0W_0-BSE:PBE0 results generally underestimate the excitation energies. In fact, the calculations on the C_4 structure using TD-PBE0, evGW-BSE:PBE0, and evGW-BSE:CAMB3LYP, produced a strong peak near 2.9 eV, indicating the possible presence of this structure in the measured spectrum. For the D_2 clusters with R = PhMe and R = PhOMe, the TD-PBE0 values for the first OPA peak are in good agreement with the experimental data, as are the evGW-BSE values with both functionals.

To better assess the agreement with the experimental data for the three clusters, the MUE relative to the experimental absorption peaks is calculated using the first five peaks of the measured

and calculated spectra (see Table 4). Since the calculations on the C_4 structure do not have the lowest energy peak, most of this analysis is for the D_2 structure; however, use of the average spectra from the two structures results in a reduction in the MUE. The averaged TD-PBE0 spectra are shown in Figure 3, as low MUE was found for all three clusters at this level of theory. However, while calculated transition energies are close to those found experimentally, the absorption intensities do not agree well, which is known to be a problem.[85] The TD-PBE0 method and both evGW calculations yield low MUEs, but comparing the measurement with our calculated values is a challenge due to many narrow peaks. The G_0W_0-BSE values are very close to the evGW-BSE results when CAMB3LYP is used, while the G_0W_0-BSE results with PBE0 typically underestimate the excitation energies. TD-CAMB3LYP results tend to over-estimate the transition energies.

Overall, comparing to the experimental optical absorption spectra,[39] the TD-PBE0 and evGW-BSE calculations on the D_2 structure model fairly well the three primary features: a low-intensity HOMO-LUMO transition near 2 eV, an intense, sharp peak near 3 eV, and a broader intense peak near 3.5 eV, although the latter shows more peak-splitting in the measured spectrum than was found in the calculations. Averaging the D_2 and C_4 spectra further improves the agreement with experiment. The experimental measurements also show small red-shifts upon modifying the

ligands with the methyl and oxymethyl groups, in agreement with our calculations, although the decreased intensities observed experimentally were not reproduced. In addition, while the two transitions near 2.5 eV have small intensities in the calculations, large intensities in the measured data are noted. Previous studies have noted the difficulties in predicting oscillator strengths.[85]

The H.R. spectrum for $Au_9(PR_3)_8^{3+}$ with R = Ph was also resolved by Fagan, et al.,[57] so we compare their resolved features to our calculated excited-states (Table S3). Since the best agreement with experiment that we obtained for this system used the average of the spectra calculated for the D_2 and C_4 structures, this analysis is less useful than it was for the Au_8 system. However, we do note a correspondence between the strong absorption observed near 2.9 eV and our calculations on the C_4 structure, as well as a correspondence in the calculations on the D_2 structure with the low-energy absorption.

Ligand effects. Our discussion on ligand effects for $Au_8(PR_3)_7^{2+}$ will focus on the evGW-BSE:PBE0 results (see Figure 4), due to the overall lowest MUE. Additional results on the calculated ligand-effects, including oscillator strengths, are shown in Figures S8-S10 for TD-PBE0, evGW-BSE:PBE0, and evGW-BSE:CAMB3LYP calculations. Calculated ligand effects in this case are quite small, particularly for R = PhMe, relative to R = Ph. The PhOMe ligand

causes a red-shift of 0.07 eV for the first peak, and a similar shift for the fourth peak. The measured ligand effects for this system were also small, with the first peak red-shifted by 0.06 eV when PhMe is substituted for Ph, and a total red-shift of 0.11 eV measured when R = PhOMe.

In considering the Hammett parameters, Cirri, et al. showed a monotonic, nearly linear red-shift in their measured first (HOMO-LUMO) transition for both $Au_8(PR_3)_7^{2+}$ and $Au_9(PR_3)_8^{3+}$, as a function of the Hammett parameter for the para substituent in the ligand. The Hammett parameter was devised intuitively to describe a relationship between chemical reaction rates, equilibrium constants, and substituents on benzoic acid,[86] and our calculated HOMO-LUMO transitions are not consistent with this simplified approach, particularly when two additional substituents, NH_2 and NO_2, are included for $Au_9(PR_3)_8^{3+}$. We list in Table S4 the Hammett parameters and the Mulliken charges on the central gold atom, calculated at the PBE0 level of theory. Previous studies suggested that electron donor ligands can contribute to an increase in electronic charge in the core of gold clusters.[87-90] This is observed here as well, with the Mulliken charge on the central gold atom for the red-shift of the HOMO-LUMO transition does follow the increase in negative charge on the central gold atom to some extent, particularly at the evGW-BSE:PBE0 level of theory.

The effect of ligands on the OPA of the D_2 $Au_9(SR)_8^{3+}$ cluster, as calculated by evGW-BSE with PBE0, is shown in Figure 5. For the cluster with R = Ph, the first peak in the calculated absorption spectrum is at 1.82 eV, due to a HOMO to LUMO transition with a small oscillator strength of 0.035. For R = PhMe and R = PhOMe, only very small red-shifts, of 0.02 and 0.03 eV, respectively, were calculated. The intensities are nearly identical for all three ligands. The 7th excited state at 3.00 eV, with a dominant contribution from the HOMO-2 to LUMO transition, but also a significant contribution from the HOMO to LUMO+2 transition, causes a more intense peak in the OPA spectrum for R = Ph due to its oscillator strength of 0.304. Changing the ligands to R = PhMe and R = PhOMe results in red-shifts of 0.05 and 0.12 eV, respectively. In this case, the intensity in the cluster with R = PhMe is slightly larger, while the oscillator strength decreases slightly for R = PhOMe. Multiple excited-states result in an even more intense peak in the near UV, and the same trend in the ligand-effects is found with a red-shift of about 0.02 eV when PhMe is substituted for Ph and a red-shift of about 0.2 eV for R = PhOMe. Calculated spectra that include two additional ligands, R = $PhNH_2$ and R = $PhNO_2$, are summarized in Figures S11-S13 in the Supplementary Material at the TD-PBE0, evGW-BSE:PBE0, and evGW-BSE:CAMB3LYP levels of theory. Table S4 includes Hammett parameters and Mulliken charges for the central gold atom

for this system with five possible ligand substituents. Surprisingly, the substituent NH_2, which as a strong electron-donor has the most negative Hammett constant, does not continue the trend of increasing red-shifting of the HOMO-LUMO transition and instead induces a blue-shift in the HOMO-LUMO transition in the evGW-BSE:PBE0 calculation and a small red-shift in the TD-PBE0 calculation. The Mulliken charge on the central gold atom has only a small change from the

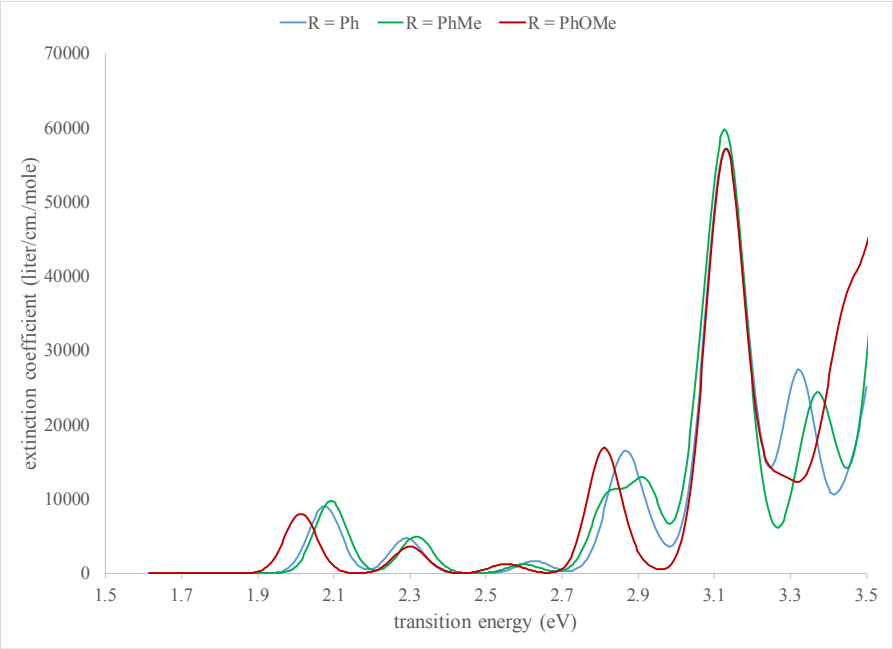

Figure 4. The effects of ligands on the OPA of $Au_8(PR_3)_7^{2+}$ calculated using evGW-BSE:PBE0. Extinction coefficients were obtained by fitting to Gaussian linewidth functions with full-width at half-maximum (FWHM) of 0.1 eV.

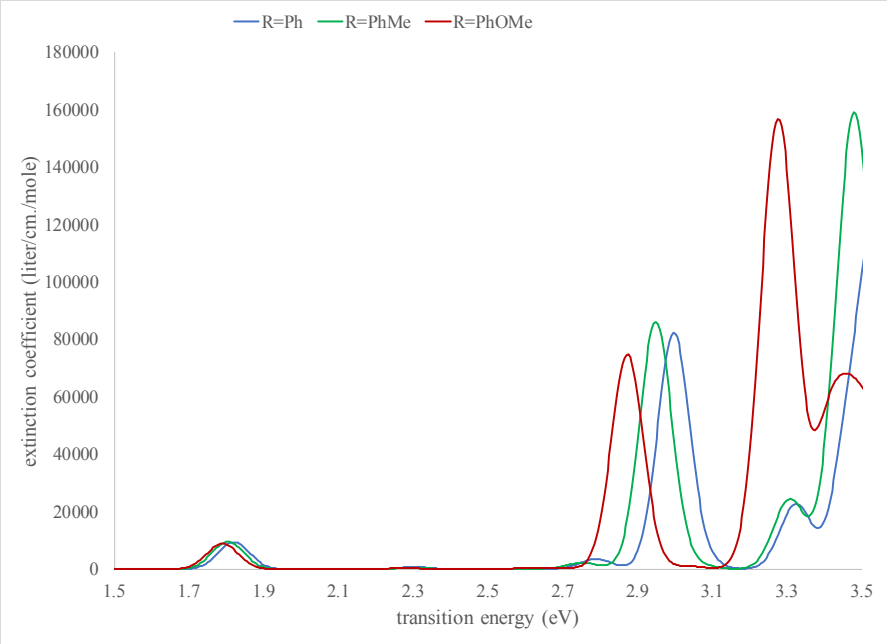

Figure 5. The effects of ligands on the OPA of the D_2 $Au_9(PR_3)_8^{3+}$ calculated using evGW-BSE with PBE0. The extinction coefficients were obtained by fitting to Gaussian linewidth functions with full-width at half-maximum (FWHM) of 0.1 eV.

para methyl substitution, but a larger change from methoxy, even larger than from the amino substituent. The nitro substituent is an electron acceptor and has a positive Hammett parameter but induces the largest increase in negative charge on the central gold atom, while causing a blue-shift in the HOMO-LUMO transition as calculated with TD-PBE0.

Analysis of the transitions in $Au_8(PR_3)_7^{2+}$ and $Au_9(PR_3)_8^{3+}$. In comparing the origin of the transitions, we note that the delocalized electrons in clusters of metal atoms can mimic atomic orbitals, filling "super-atom" orbitals in the order $1S^2$ | $1P^6$ | $1D^{10}$ | $2S^2$ $1F^{14}$ | $2P^6$ $1G^{18}$| $2D^{10}$ $3S^2$ $1H^{22}$, with each gold atom contributing one electron to the super-atom orbital, as was introduced

by Walter, et al.[91] The super-atom character of a molecular orbital is identified by its shape and symmetry similar to the analogous atomic orbital. While thiol ligands are considered electron withdrawing, phosphine ligands are considered weak surfactants, neither withdrawing nor donating electrons. Super-atom theory has worked well in predicting the stability and properties of clusters, particularly those with spherical symmetry,[81,92] such as $Au_{25}(SR)_{18}$-. However, for systems with more deviation from spherical symmetry such as the clusters studied here, this assumption may not be appropriate.

Figure 6 shows the HOMO and LUMO orbitals calculated for the D_2 $Au_9(PR_3)_8^{3+}$ using PBE0 with R = Ph, and R = PhOMe, In this case, we found that the orbitals with super-atom P character include HOMO-1, HOMO, and LUMO+1, while orbitals with D character include LUMO, LUMO+2 and LUMO+4. This is consistent with a previous report using TDDFT with the LB94 functional[30] for this system with R = Ph, except that the D character with LUMO+4 was not identified, and the P-like orbital character that was demonstrated in Ref.[30] for HOMO-2, we found for HOMO-1. Using PBE0 we found the HOMO-2 to have primarily localized d_z^2 structures on gold atoms, while HOMO-3 and HOMO-4 have localized d structures on gold atoms and ligand

atoms. The LUMO+3 orbital has some superatom F character, which is important for two-photon absorption, as discussed in the following.

Table S5 lists the orbitals for the dominant transition for the excited states of this cluster. The first excited state is largely due to the HOMO→LUMO transition (1P to 1D) and has a modest oscillator strength of about 0.03. Excited-states 2 and 4 result from 1P to 1P transitions, which are forbidden, and excited state 6 is characterized by a P to F transition, also forbidden. Excited-states 3 and 5 involve 1P to 1D transitions, and have low oscillator strengths. Excited-state 7 produces the strong peak at about 3.1 eV, due to a combination of HOMO-2→LUMO (d_z^2 to 1D) and HOMO→LUMO+2 (1P to 1D). For R = PhOMe, the super-atom orbital structure is largely consistent with that found for R = Ph, and characterization of the transitions in the spectrum matches for the first 4 excited states, but the 5th excited state is due to HOMO-2→LUMO instead of HOMO→LUMO+2; the strong transition is now the 6th excited state, dominated by HOMO→LUMO+2, the 7th excited state from HOMO-4→LUMO is very weak, and the 9th excited state involves the transition to the superatom F orbital.

In Figure 7 we show these orbitals for $Au_8(PR_3)_7^{2+}$. This system, while also having six delocalized electrons, has considerably less symmetry and thus the super-atom theory could be

less useful. While the distortion from the shape of the analogous atomic orbitals is larger, the HOMO-1, HOMO, and LUMO+1 all have some super-atom P character, but also with significant contributions from local d orbitals. The LUMO and LUMO+2 have some super-atom 1D-like structure, but also significant local d structure. The first excited-state is due to the HOMO→LUMO transition and the second excited-state to the HOMO-1→LUMO. Both

a)

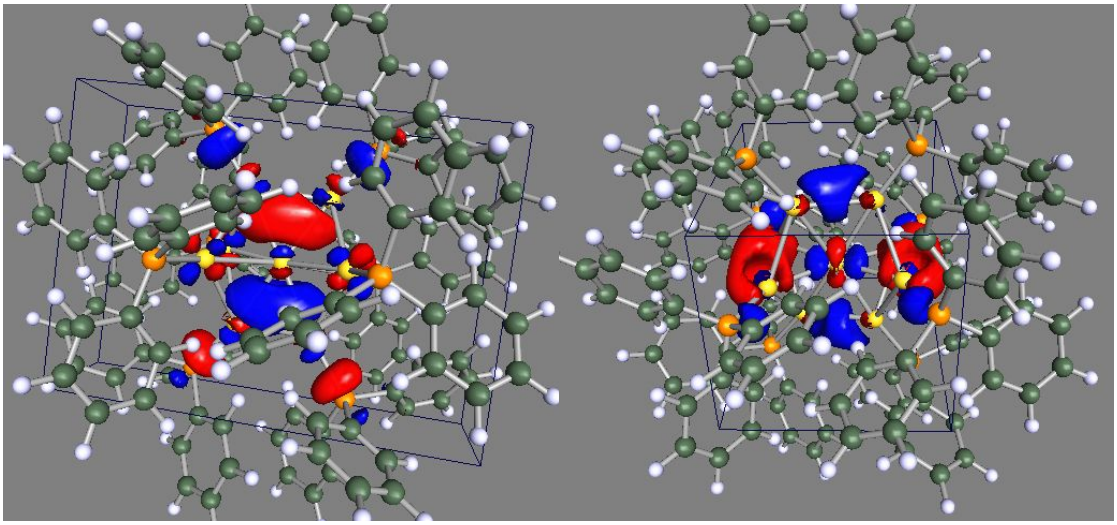

b)

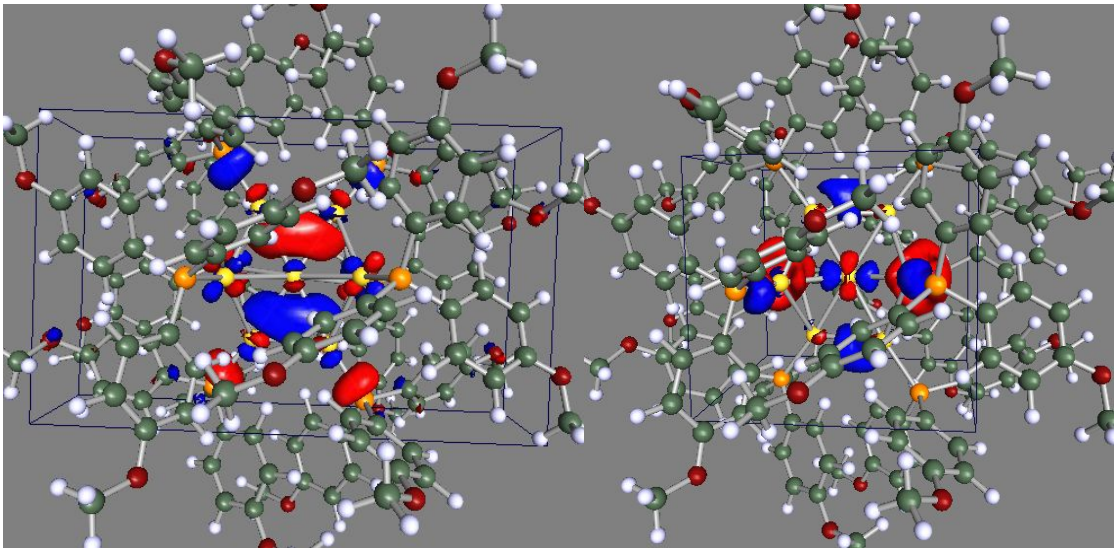

Figure 6. The HOMO (left) and LUMO (right) calculated using the PBE0 X-C functional for the D_2 $Au_9(PR_3)_8^{3+}$ with a) R = Ph and b) R=PhOMe.

transitions have moderate intensities and could be described as 1P→1D. The third excited-state is due to the HOMO→LUMO+1 transition and while its intensity is small, it is not so low as to be described as "forbidden", as would be predicted for a 1P→1P transition. Thus, the super-atom

model does not describe the absorption for the Au_8 system as well as for the Au_9 system. The higher excited-states have contributions from multiple orbital transitions, making the super-atom description even less likely to be applicable.

In addition to the calculated HOMO and LUMO energies, the calculated excitation energy to the first excited-state, S1, using TDDFT and evGW-BSE with the PBE0 functional, is also summarized in Table S4. For the R = Ph ligands, the geometry of the S1 state was optimized, allowing for the calculation of ΔE, namely the difference in energy between the optimized S0 and S1 states, compared to the vertical emission energy. While the vertical absorption energy is often used as a good approximation to the measured absorption energy, the absorption energy could be as low as ΔE, depending on the Franck-Condon factors. For these systems, the vertical absorption energy predicts the position of the first experimental peak more accurately than does ΔE. The fluorescence energy is often approximated by ΔE, but could be as low as the vertical emission energy. Thus for $Au_9(PPh_3)_8^{3+}$, this calculation predicts fluorescence in the range 1.22 – 1.59 eV, which is consistent with the low-energy emission observed previously at 1.45 eV (853 nm).[27]

Two-Photon Absorption: $Au_8(PR_3)_7^{2+}$ and ***$Au_9(PR_3)_8^{3+}$.*** Since TPA materials are in demand for a variety of applications and some gold clusters have been reported to have large TPA, we are also reporting a purely theoretical investigation of the TPA for these clusters. The calculated TPA

spectra for the $Au_8(PR_3)_7^{2+}$ clusters are shown in Figures 8. The maximum transition energy of 3.7 eV is below twice the energy of the first excited-state to avoid resonance effects in the calculations and to avoid linear absorption interference in applications. This maximum corresponds to two photons with energy 1.85 eV, corresponding to a wavelength of 670 nm. The $Au_8(PR_3)_7^{2+}$ cluster has a modest TPA cross-section that can be affected by the ligand. When R = Ph, a small TPA peak of 11 GM is predicted at a transition energy of 3.01 eV (corresponding to two photons of

a)

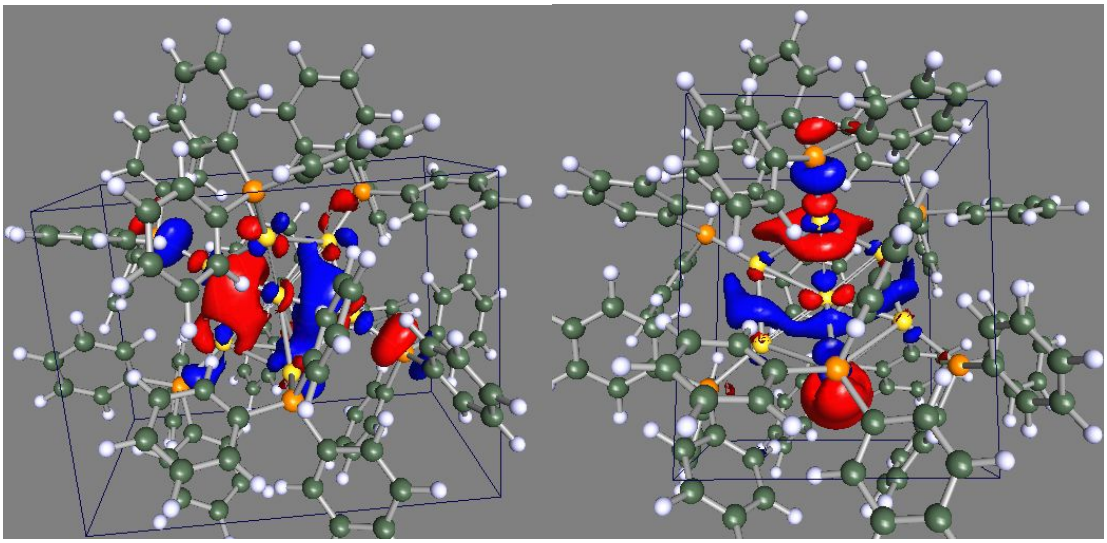

b)

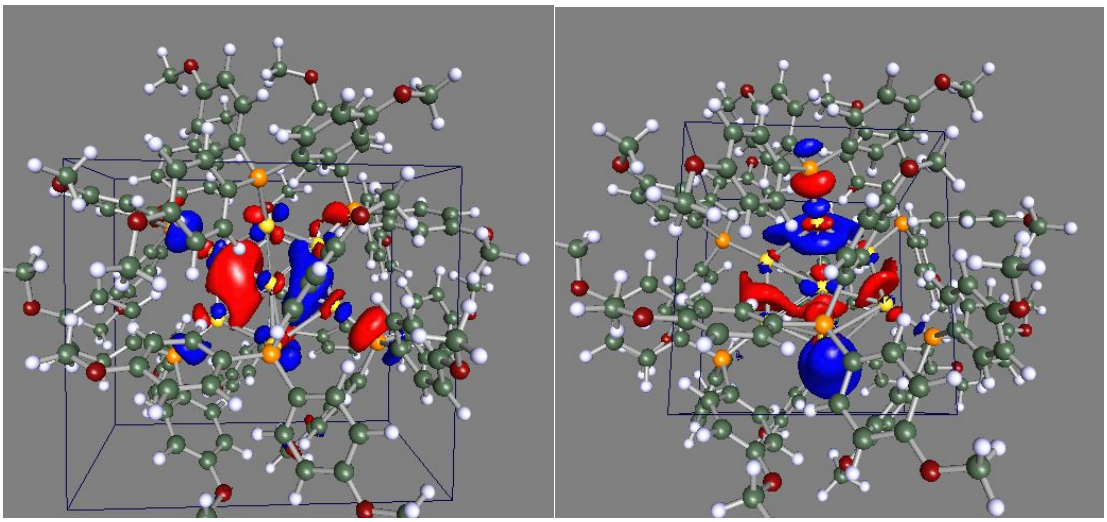

Figure 7. The HOMO (left) and LUMO (right) calculated using the PBE0 X-C functional for $Au_8(PR_3)_7^{2+}$ with a) R = Ph and b) R=PhOMe.

1.51 eV, or 823 nm), which is only slightly increased to 13 GM and red-shifted to 2.99 eV (corresponding to 830 nm) when R = PhOMe. When R = PhMe, this peak is at 2.98 eV and is 11 GM. From the SOS expression, Equation (3), we see that in order for a term to contribute to the

TPA cross-section for final state *f*, two transition dipole moments must be non-zero: μ_{j0} (between the ground-state and the intermediate excited-state *j*) and μ_{fj} (between the intermediate state *j* and the final state *f*). For this first TPA peak with R=PhMe, the final state is $f = 6$ at 2.99 eV. The most likely intermediate state for the dominant term is $j = 1$, at 2.19 eV.

The primary orbitals in this TPA mechanism are shown in Figure S14. The transition from the ground-state to the first excited state ($j = 1$) is a HOMO to LUMO transition, corresponding to superatom orbitals P_x to D_{z2}, an allowed transition following the $\Delta J = \pm 1$ rule, and confirmed by our calculations with $f_{10} = 0.0383$ ($\mu_{10} = 0.844$ in atomic units). The excitation to $f = 6$ involves a transition to the LUMO + 3 orbital, which has some superatom F character, thus we expect μ_{61} to be non-zero since it involves a D to F transition. The term with $j = 2$ could also contribute to this TPA peak since it also involves a transition from a superatom P to D (HOMO - 1 to LUMO), although its contribution is likely smaller since the oscillator strength is smaller and the energy difference in the denominator of Equation (3) is greater. Each of the $Au_8(PR_3)_7^{2+}$ clusters, with R =Ph, PhMe, and PhOMe, has a second TPA peak; the transition energies are 3.23 eV, 3.21 eV, and 3.22 eV and the TPA cross-sections are 7 GM, 10 GM, and 12 GM, respectively. For R = PhMe, this peak is from a transition to f = 8 at 3.21 eV, which also involves a transition to the F-like

orbital LUMO + 3, so a similar mechanism, starting instead with the H-1 with P_y character, can describe this TPA peak. The transitions producing the higher energy TPA peaks are too complex to be explained with superatom theory. While the R = Ph cluster has peaks of 53 GM and 96 GM at 3.47 eV (715 nm) and 3.67 eV (676 nm), respectively, the R = PhOMe cluster has one intense peak of 137 GM at 3.55 eV (699 nm). The calculated TPA

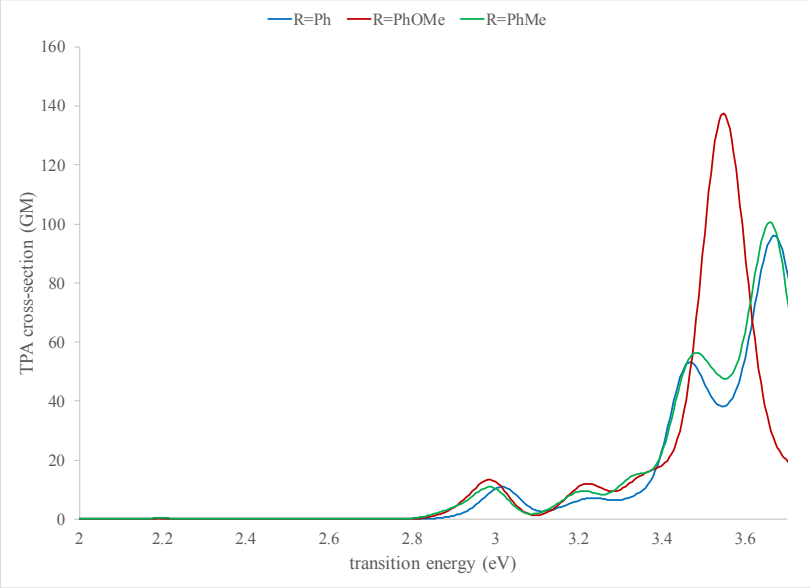

Figure 8. Calculated TPA for $Au_8(PR_3)_7^{2+}$ using quadratic response TD-PBE0 and a Gaussian linewidth of 0.1 eV.

spectrum with R = PhMe is quite similar to that with R = Ph. Thus, in some cases, the ligand can be used to tune TPA.

The calculated TPA of the $Au_9(PR_3)_8^{3+}$ cluster (Figure 9) is more complicated due to the two isomers for this cluster. For R = Ph, the calculation on the D_2 isomer predicts peaks at 3.08 eV (806 nm), 3.35 eV (741 nm), and 3.55 eV (698 nm) with TPA cross-sections of 45 GM, 71 GM, and 400 GM respectively; however, the prediction for the C_4 isomer shows a small cross-section, with a peak of about 8 GM at 3.45 eV (719 nm). Substituting the Ph ligands in the D_2 isomer with PhOMe causes a red-shift of the peaks with a decrease in the maximum absorption cross-section, which is similar to the results of the linear absorption calculations. We predict peaks at 3.01 eV (823 nm), 3.18 eV (780 nm), and 3.46 eV (716 nm) with TPA cross-sections of 112 GM, 256 GM, and 115 GM, respectively. The C_4 isomer shows larger values in this energy range when R = PhOMe, with peaks at 3.12 eV (794 nm), 3.31 eV (748 nm), and 3.55 eV (699 nm) having TPA cross-sections of 42 GM, 75 GM, and 147 GM.

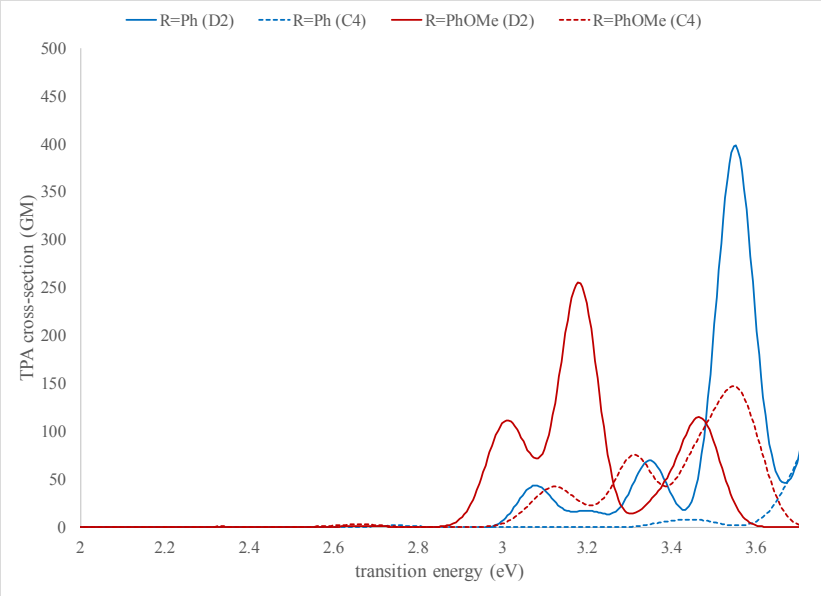

Figure 9. Calculated TPA for $Au_9(PR_3)_8^{3+}$ using quadratic response TD-PBE0 and a Gaussian linewidth of 0.1 eV.

In the D_2 structures, the LUMO+3 orbital has superatom F character, and the first TPA peak can be described, similar to the above description in the Au_8 cluster, by a superatom P to D to F transition, with the first excited-state acting as the virtual-state and the 6th excited-state as the final state when R=Ph. The key orbitals in this mechanism are shown in Figure S15. When R = PhOMe there is also the P to D to F transition with the 8th excited-state at 3.01 eV acting as the final state, but the 7th and 9th excited-states also act as final states with significant TPA contributing to the peak at 3.01 eV. For each ligand, the excited states from the H-3→L, H-4→L, H-5→L, and H-6→L orbital transitions are all weak OPA states but have significant TPA. For $Au_9(PR_3)_8^{3+}$ there

is also the possibility of fine-tuning the TPA through ligand substitution, or by controlling the fraction of each isomer present.

Conclusions

In summary, the structures have been optimized using DFT, and the absorption spectra were calculated at the TDDFT and GW-BSE levels of theory for the $Au_8(PR_3)_7^{2+}$ and $Au_9(PR_3)_8^{3+}$ clusters, which have been characterized experimentally. Using the average Au-Au bond length as a guide, the crystal structure geometry for each system was found to be more compact than the calculated structures. Our PBE0-D3 geometries were closest to the crystal structure, improving on previously reported DFT structures. The OPA spectra using TDDFT with PBE0 are in fair agreement with the measured absorption, while TDDFT with CAMB3LYP over-estimates the excitation energies. Using the evGW-BSE method improves the agreement with experiment. In particular, values for the MUE calculated using evGW-BSE:PBE0 on $Au_8(PR_3)_7^{2+}$ with R = Ph, PhMe, and PhOMe were 0.08 eV, 0.07 eV, and 0.07 eV, respectively, although the agreement with experimental intensities was not as good, as is well-known.[85] While the MUE was similarly low when using TD-PBE0, the evGW-BSE method has the advantage of less dependence on the exchange-correlation functional. We find that averaging our calculated spectra for the D_2 and C_4

isomers of the $Au_9(PR_3)_8^{3+}$ cluster demonstrates the best agreement with experiment, potentially indicating the possible presence of both isomers in the measured sample. Replacing the ligand R = Ph with R = PhMe was a small red-shift in the OPA, while R = PhOMe produced a larger red-shift, which is consistent with experiment. Superatom orbitals with P, D, and F character could partially explain or predict the OPA and TPA, particularly in the D_2 $Au_9(PR_3)_8^{3+}$ structure. Also, for $Au_9(PR_3)_8^{3+}$, TPA is stronger from the D_2 isomer than from the C_4 isomer.

Supplementary Material

The Supplementary Material contains a table with additional measured and calculated absorption features, a table listing calculated transition energies, oscillator strengths, and corresponding orbitals, a table with orbital energies and energetics from excited-state optimizations, figures showing the absorption spectra calculated at the different levels of theory with comparison to experiment, additional plots showing the calculated ligand effects on the absorption spectra, figures showing the key orbitals in TPA, figures showing the full structure of each cluster studied here, and the Cartesian coordinates of the optimized geometries for these clusters.

Conflicts of interest

There are no conflicts to declare.

Acknowledgements

We gratefully acknowledge support by the Air Force Office of Scientific Research (AFOSR) and the resources and helpful assistance provided by the AFRL DoD Supercomputing Resource Center. Special thanks to Prof. Christopher Johnson, Stony Brook University, for fruitful discussions.

References

(1) Natarajan, G.; Mathew, A.; Negishi, Y.; Whetten, R. L.; Pradeep, T. A Unified Framework for Understanding the Structure and Modifications of Atomically Precise Monolayer Protected Gold Clusters. *J. Phys. Chem. C* **2015**, *119*, 27768−27785.

(2) Chakraborty, I.; Pradeep, T. Atomically Precise Clusters of Noble Metals: Emerging Link between Atoms and Nanoparticles. *Chem. Rev.* **2017**, *117*, 8208-8271.

(3) Sumner, L.; Sakthivel, N. A.; Schrock, H.; Artyushkova, K.; Dass, A.; Chakraborty, S. Electrocatalytic Oxygen Reduction Activities of Thiol-Protected Nanomolecules Ranging in Size from $Au_{28}(SR)_{20}$ to $Au_{279}(SR)_{84}$. *J. Phys. Chem. C* **2018**, *122*, 24809−24817.

(4) Kang, X.; Li, Y.; Zhu, M.; Jin, R. Atomically precise alloy nanoclusters: syntheses, structures, and properties. *Chem. Soc. Rev.* **2020**, *49*, 6443-6514.

(5) Konishi, K.; Iwasaki, M.; Shichibu, Y. Phosphine-Ligated Gold Clusters with Core+exo Geometries: Unique Properties and Interactions at the Ligand−Cluster Interface. *Acc. Chem. Res.* **2018**, *51*, 3125−3133.

(6) Ackerson, C. J.; Powell, R. D.; Hainfeld, J. F. Site-specific Biomolecule Labeling with Gold Clusters. *Methods Enzymol* **2010**, *481*, 195-230.

(7) Abbas, M. A.; Kamat, P. V.; Bang, J. H. Thiolated Gold Nanoclusters for Light Energy Conversion. *ACS Energy Lett.* **2018**, *3*, 840−854.

(8) Aikens, C. M. Electronic and Geometric Structure, Optical Properties, and Excited State Behavior in Atomically Precise Thiolate-Stabilized Noble Metal Nanoclusters. *Acc. Chem. Res.* **2018**, *51*, 3065−3073.

(9) Kang, X.; Chong, H.; Zhu, M. $Au_{25}(SR)_{18}$: the Captain of the Great Nanocluster Ship. *Nanoscale* **2018**, *10*, 10758-10834.

(10) Kang, X.; Zhu, M. Tailoring the Photoluminescense of Atomically Precise Nanoclusters. *Chem. Soc. Rev.* **2019**, *48*, 2422-2457.

(11) Day, P. N.; Pachter, R.; Nguyen, K. A.; Jin, R. Theoretical Prediction of Optical Absorption and Emission in Thiolated Gold Clusters. *J. Phys. Chem. A* **2019**, *123*, 6472−6481.

(12) Zeng, C.; Li, C.; Chen, Y.; Rosi, N. L.; Jin, R. Gold−Thiolate Ring as a Protecting Motif in the $Au_{20}(SR)_{16}$ Nanocluster and Implications. *J. Am. Chem. Soc.* **2014**, *136*, 11922−11925.

(13) Gutrath, B. S.; Englert, U.; Wang, Y.; Simon, U. A Missing Link in Undecagold Cluster Chemistry: Single-Crystal X-ray Analysis of $[Au_{11}(PPh_3)_7Cl_3]$. *Eur. J. Inorg. Chem.* **2013**, *2013*, 2002–2006.

(14) Hall, K. P.; Theoblad, B. R.; Gilmour, D. I.; Mingos, D. M. P.; Welch, A. J. Synthesis and structural characterization of $[Au_9(P(p\text{-}C_6H_4OMe)_3)_8](BF_4)_3$; a cluster with a centred crown of gold atoms. *J. Chem. Soc., Chem. Commun.* **1982**, *1982*, 528-530.

(15) Zhang, S.-S.; Feng, L.; Senanayake, R. D.; Aikens, C. M.; Wang, X.-P.; Zhao, Q.-Q.; Tunga, C.-H.; Sun, D. Diphosphine-protected ultrasmall gold nanoclusters: opened icosahedral Au_{13} and heartshaped Au_8 clusters. *Chem. Sci.* **2018**, *9*, 1251–1258.

(16) Wan, X.-K.; Lin, Z.-W.; Wang, Q.-M. Au_{20} Nanocluster Protected by Hemilabile Phosphines. *J. Am. Chem. Soc.* **2012**, *134*, 14750−14752.

(17) Chen, J.; Zhang, Q.-F.; Williard, P. G.; Wang, L.-S. Synthesis and Structure Determination of a New Au_{20} Nanocluster Protected by Tripodal Tetraphosphine Ligands. *Inorg. Chem.* **2014**, *53*, 3932−3934.

(18) Pei, Y.; Gao, Y.; Zeng, X. C. Structural Prediction of Thiolate-Protected Au_{38}: A Face-Fused Bi-icosahedral Au Core. *J. Am. Chem. Soc.* **2008**, *130*, 7830–7832.

(19) Qian, H.; Eckenhoff, W. T.; Zhu, Y.; Pintauer, T.; Jin, R. Total Structure Determination of Thiolate-Protected Au_{38} Nanoparticles. *J. Am. Chem. Soc.* **2010**, *132*, 8280-8281.

(20) Higaki, T.; Li, Q.; Zhou, M.; Zhao, S.; Li, Y.; Li, S.; Jin, R. Toward the Tailoring Chemistry of Metal Nanoclusters for Enhancing Functionalities. *Accounts of Chemical Research* **2018**, *51*, 2764-2773.

(21) Weerawardene, K. L. D. M.; Guidez, E. B.; Aikens, C. M. Photoluminescence Origin of $Au_{38}(SR)_{24}$ and $Au_{22}(SR)_{18}$ Nanoparticles: A Theoretical Perspective. *J. Phys. Chem. C* **2017**, *121*, 15416−15423.

(22) McPartlin, M.; Mason, R.; Malatesta, L. Novel Cluster Complexes of Gold(0)-Gold(I). *J. Chem. Soc. D* **1969**, *0*, 334-334.

(23) Albano, V. G.; Bellon, P. L.; Manassero, M.; Sansoni, M. Intermetallic Pattern in Metal-Atom Clusters. Structural Studies on $Au_{11}X_3(PR_3)_7$ Species. . *J. Chem. Soc. D* **1970**, *0*, 1210−1211.

(24) Shichibu, Y.; Suzuki, K.; Konishi, K. Facile synthesis and optical properties of magic-number Au_{13} clusters. *Nanoscale* **2012**, *4*, 4125–4129.

(25) Shichibu, Y.; Konishi, K. HCl-Induced Nuclearity Convergence in Diphosphine-Protected Ultrasmall Gold Clusters: A Novel Synthetic Route to ''Magic-Number'' Au_{13} Clusters. *Small* **2010**, *6*, 1216-1220.

(26) Hall, K. P.; Mingos, D. M. P.: Homo- and Heteronuclear Cluster Compounds of Gold. In *Progress in Inorganic Chemistry*; Lippard, S. J., Ed., 1984; Vol. 32; pp 237-325.

(27) Wen, F.; Englert, U.; Gutrath, B.; Simon, U. Crystal Structure, Electrochemical and Optical Properties of $[Au_9(PPh_3)_8](NO_3)_3$. *Eur. J. Inorg. Chem.* **2008**, *2008*, 106-111.

(28) Jaw, H.-R. C.; Mason, W. R. Electronic Absorption and MCD Spectra for the $Au_8(PPh_3)_8^{2+}$ Ion. *Inorg. Chem.* **1991**, *30*, 3552-3555.

(29) Jaw, H.-R. C.; Mason, W. R. Magnetic Circular Dichroism Spectra for the $Au_9(PPh_3)_8^{3+}$ Ion. *Inorg. Chem.* **1991**, *30*, 275-278.

(30) Karimova, N. V.; Aikens, C. M. Time Dependent Density Functional Theory Study of Magnetic Circular Dichroism Spectra of Gold Clusters $Au_9(PH_3)_8^{3+}$ and $Au_9(PPh_3)_8^{3+}$. *J. Phys. Chem. A* **2016**, *120*, 9625-9635.

(31) Madridejos, J. M. L.; Harada, T.; Falcinella, A. J.; Small, T. D.; Golovko, V. B.; Andersson, G. G.; Metha, G. F.; Kee, T. W. Optical Properties of the Atomically Precise C_4 Core $[Au_9(PPh_3)_8]^{3+}$ Cluster Probed by Transient Absorption Spectroscopy and Time-Dependent Density Functional Theory. *J. Phys. Chem. C* **2021**, *125*, 2033−2044.

(32) Yamazoe, S.; Matsuo, S.; Muramatsu, S.; Takano, S.; Nitta, K.; Tsukuda, T. Suppressing Isomerization of Phosphine-Protected Au_9 Cluster by Bond Stiffening Induced by a Single Pd Atom Substitution. *Inorg. Chem.* **2017**, *56*, 8319−8325.

(33) Wei, J.; Rodríguez-Kessler, P. L.; Halet, J.-F. o.; Kahlal, S.; Saillard, J.-Y.; Muñoz-Castro, A. On Heteronuclear Isoelectronic Alternatives to $[Au_{13}(dppe)_5Cl_2]_{3+}$: Electronic and Optical Properties of the 18-Electron $Os@[Au_{12}(dppe)_5Cl_2]$ Cluster from Relativistic Density FunctionalTheory Computations. *Inorg. Chem.* **2021**, *60*, 8173−8180.

(34) Jianyu Wei, J.-F. o. H.; Kahlal, S.; Saillard, J.-Y.; Muñoz-Castro, A. Toward the Formation of N-Heterocyclic-Carbene-Protected Gold Clusters of Various Nuclearities. A Comparison with Their Phosphine-Protected Analogues from Density Functional Theory Calculations. *Inorg. Chem.* **2020**, *59*, 15240−15249.

(35) Muñoz-Castro, A. Potential of N-heterocyclic carbene derivatives from $Au_{13}(dppe)_5Cl_2$ gold superatoms. Evaluation of electronic, optical and chiroptical properties from relativistic DFT. *Inorg. Chem. Front.* **2019**, *6*, 2349–2358.

(36) Carey, D. M.; Muñoz-Castro, A. Evaluation of N-Heterocyclic Carbene Counterparts of Classical Gold Clusters; Bonding Properties of Octahedral CAu_6, Icosahedral $Au_{13}Cl_2$, and Bi-icosahedral $Au_{25}Cl_2$ Cores from Relativistic DFT Calculations. *J. Phys. Chem. C* **2019**, *123*, 12466−12473.

(37) Ai, P.; Mauro, M.; Danopoulos, A. A.; Muñoz-Castro, A.; Braunstein, P. Dual Emission of a Cyclic Hexanuclear Gold(I) Complex. Interplay between Au_3 and Au_2 Ligand-Supported Luminophores. *J. Phys. Chem. C* **2019**, *123*, 915−921.

(38) Cirri, A.; Hernandez, H. M.; Kmiotek, C.; Johnson, C. J. Systematically Tuning the Electronic Structure of Gold Nanoclusters through Ligand Derivatization. *Angew. Chem. Int. Ed.* **2019**, *58*, 13818 –13822.

(39) Cirri, A.; Hernández, H. M.; Johnson, C. J. High Precision Electronic Spectroscopy of Ligand-Protected Gold Nanoclusters: Effects of Composition, Environment, and Ligand Chemistry. *J. Phys. Chem. A* **2020**, *124*, 1467−1479.

(40) Ye, J.; Ma, L.-S.; Hall, J. L. Ultrasensitive detections in atomic and molecular physics: demonstration in molecular overtone spectroscopy. *J. Opt. Soc. Am. B* **1998**, *15*, 6-15.

(41) Laurent, A. D.; Jacquemin, D. TD-DFT benchmarks: A review. *Int. J. Quantum Chem.* **2013**, *113*, 2019-2039.

(42) Hedin, L. New method for calculating the one-particle Green's function with application to the electron-gas problem. *Physical Review* **1965**, *139 (3A)*, 796-823.

(43) Hybertsen, M. S.; Louie, S. G. Electron correlation in semiconductors and insulators: band gaps and quasiparticle energies. *Phys. Rev. B: Condens. Matter* **1986**, *34*, 5390-5413.

(44) vanSetten, M. J.; Weigend, F.; Evers, F. The GW-Method for Quantum Chemistry Applications: Theory and Implementation. *J. Chem. Theory Comput.* **2013**, *9*, 232−246.

(45) Qiu, D. Y.; da Jornada, F. H.; Louie, S. G. Optical spectrum of MoS2: many-body effects and diversity of exciton states. *Phys. Rev. Lett.* **2013**, *111*, 216805/216801-216805/216805.

(46) Thygesen, K. S. Calculating excitons, plasmons, and quasiparticles in 2D materials and van der Waals heterostructures. *2D Materials* **2017**, *4*, 022004.

(47) Jiang, J.; Pachter, R.; Mou, S. Tunability in the optical response of defective monolayer WSe2 by computational analysis. *Nanoscale* **2018**, *10*, 13751-13760.

(48) Loh, L.; Chen, Y.; Wang, J.; Yin, X.; Tang, C. S.; Zhang, Q.; Watanabe, K.; Taniguchi, T.; Wee, A. T.; Bosman, M. Impurity-Induced Emission in Re-Doped WS2 Monolayers. *Nano Letters* **2021**.

(49) Krause, K.; Klopper, W. Implementation of the Bethe-Salpeter Equation in the TURBOMOLE Program. *J. Comput. Chem.* **2017**, *38*, 383-388.

(50) Marom, N.; Caruso, F.; Ren, X.; Hofmann, O. T.; Körzdörfer, T.; Chelikowsky, J. R.; Rubio, A.; Scheffler, M.; Rinke, P. Benchmark of G W methods for azabenzenes. *Physical Review B* **2012**, *86*, 245127.

(51) Faber, C.; Boulanger, P.; Attaccalite, C.; Duchemin, I.; Blase, X. Excited states properties of organic molecules: from density functional theory to the GW and Bethe-Salpeter Green's function formalisms. *Philos. Trans. R. Soc., A* **2014**, *372*, 20130271/20130271-20130271/20130218.

(52) Kaplan, F.; Harding, M. E.; Seiler, C.; Weigend, F.; Evers, F.; Setten, M. J. v. Quasi-Particle Self-Consistent GW for Molecules. *J. Chem. Theory Comput.* **2016**, *12*, 2528−2541.

(53) Jacquemin, D.; Duchemin, I.; Blase, X. Benchmarking the Bethe−Salpeter Formalism on a Standard Organic Molecular Set. *J. Chem. Theory Comput.* **2015**, *11*, 3290−3304.

(54) Boulanger, P.; Chibani, S.; Guennic, B. L.; Duchemin, I.; Blase, X.; Jacquemin, D. Combining the Bethe−Salpeter Formalism with Time-Dependent DFT Excited-State Forces to Describe Optical Signatures: NBO Fluoroborates as Working Examples. *J. Chem. Theory Comput.* **2014**, *10*, 4548−4556.

(55) Briant, C. E.; Hall, K. P.; Mingos, D. M. P. Structural Characterisation of Two Crystalline Modifications of $[Au_9\{P(C_6H_40Me\text{-}p)_3\}_8](NO_3)_3$: the First Example of Skeletal Isomerism in Metal Cluster Chemistry. *Chem. Soc., Chem. Commun.* **1984**, 290-291.

(56) Mason, W. R. Electronic Absorption and MCD Spectra for $Pt(AuPPh_3)_8^{2+}$ and $Au(AuPPh_3)_8^{3+}$ Cluster Complexes in Poly(methyl methacrylate) Thin Films at 295 and 10 K. *Inorg. Chem.* **2000**, *39*, 370-374.

(57) Fagan, J. W.; Weerawardene, K. L. D. M.; Cirri, A.; Aikens, C. M.; Johnson, C. J. Toward quantitative electronic structure in small gold nanoclusters. *J. Chem. Phys.* **2021**, *155*, 014301.

(58) Grüning, M.; Gritsenko, O.; Van Gisbergen, S.; Baerends, n. E. Shape corrections to exchange-correlation potentials by gradient-regulated seamless connection of model potentials for inner and outer region. *The Journal of Chemical Physics* **2001**, *114*, 652-660.

(59) Ebina, M.; Iwasa, T.; Harabuchi, Y.; Taketsugu, T. Time-Dependent Density Functional Theory Study on Higher Low-Lying Excited States of $Au_{25}(SR)_{18}^-$ *J. Phys. Chem. C* **2018**, *122*, 4097−4104.

(60) Jiang, D.-e.; Kühn, M.; Tang, Q.; Weigend, F. Superatomic Orbitals under Spin−Orbit Coupling. *J. Phys. Chem. Lett.* **2014**, *5*, 3286-3289.

(61) Jacquemin, D.; Duchemin, I.; Blase, X. 0−0 Energies Using Hybrid Schemes: Benchmarks of TD-DFT, CIS(D), ADC(2), CC2, and BSE/GW formalisms for 80 Real-Life Compounds. *J. Chem. Theory Comput.* **2015**, *11*, 5340−5359.

(62) Ramakrishna, G.; Varnavski, O.; Kim, J.; Lee, D.; Goodson, T. Quantum-Sized Gold Clusters as Efficient Two-Photon Absorbers. *J. Am. Chem. Soc.* **2008**, *130*, 5032-5033.

(63) Ramakrishna, G.; Varnavskia, O.; Kimb, J.; Leeb, D.; Goodson, T. In *Nonlinear Optical Properties of Quantum Sized Gold Clusters*, Linear and Nonlinear Optics of Organic Materials VIII, San Diego, California, USA 28 Aug. , 2008; Jakubiak, R.; SPIE - The International Society for Optical Engineering 2008.

(64) Weigend, F.; Ahlrichs, R. Balanced Basis Sets of Split Valence, Triple Zeta Valence and Quadruple Zeta Valence Quality for H to Rn: Design and Assessment of Accuracy. *Phys. Chem. Chem. Phys.* **2005**, *7*, 3297-3305.

(65) Frisch, M. J.; Trucks, G. W.; Schlegel, H. B.; Scuseria, G. E.; Robb, M. A.; Cheeseman, J. R.; Scalmani, G.; Barone, V.; Mennucci, B.; Petersson, G. A.; Nakatsuji, H.; Caricato, M.; Li, X.; Hratchian, H. P.; Izmaylov, A. F.; Bloino, J.; Zheng, G.; Sonnenberg, J. L.; Hada, M.; Ehara, M.; Toyota, K.; Fukuda, R.; Hasegawa, J.; Ishida, M.; Nakajima, T.; Honda, Y.; Kitao, O.; Nakai, H.; Vreven, T.; J. A. Montgomery, J.; Peralta, J. E.; Ogliaro, F.; Bearpark, M.; Heyd, J. J.; Brothers, E.; Kudin, K. N.; Staroverov, V. N.; Keith, T.; Kobayashi, R.; Normand, J.; Raghavachari, K.; Rendell, A.; Burant, J. C.; Iyengar, S. S.; Tomasi, J.; Cossi, M.; Rega, N.; Millam, J. M.; Klene, M.; Knox, J. E.; Cross, J. B.; Bakken, V.; Adamo, C.; Jaramillo, J.; Gomperts, R.; Stratmann, R. E.; Yazyev, O.; Austin, A. J.; Cammi, R.; Pomelli, C.; Ochterski, J. W.; Martin, R. L.; Morokuma, K.; Zakrzewski, V. G.; Voth, G. A.; Salvador, P.; Dannenberg, J. J.; Dapprich, S.; Daniels, A. D.; Farkas, O.; J. B. Foresman; J. V. Ortiz; Cioslowski, J.; Fox, D. J.: Gaussian 16. A.03 ed.; Gaussian, Inc.: Wallingford CT, 2016.

(66) Adamo, C.; Barone, V. Acurate Excitation Energies from Time-Dependent Density Functional Theory: Assessing the PBEO Model for Organic Free Radical. *Chem. Phys. Lett.* **1999**, *314*, 152-157.

(67) Grimme, S.; Antony, J.; Ehrlich, S.; Krieg, H. A Consistent and Accurate Ab Initio Parametrization of Density Functional Dispersion Correction (DFT-D) for the 94 Elements H-Pu. *Journal of Chemical Physics* **2010**, *132*, 154104.

(68) Ahlrichs, R.; Baer, M.; Haeser, M.; Horn, H.; Koelmel, C. Electronic structure calculations on workstation computers: the program system TURBOMOLE. *Chem. Phys. Lett.* **1989**, *162*, 165-169.

(69) Furche, F.; Ahlrichs, R.; Hättig, C.; Klopper, W.; Sierka, M.; Weigend, F. Turbomole. *WIREs Comput. Mol. Sci.* **2014**, *4*, 91-100.

(70) Holzer, C.; Klopper, W. Ionized, electron-attached, and excited states of molecular systems with spin–orbit coupling: Two-component GW and Bethe–Salpeter implementations. *J. Chem. Phys.* **2019**, *150*, 204116

(71) Furche, F.; Rappoport, D.: Density functional methods for excited states: equilibrium structure and electronic spectra. In *Computational Photochemistry*; Olivucci, M., Ed. Theoretical and Computational Chemistry; Elsevier: Amsterdam, 2005; Vol. 16.

(72) Bauernschmitt, R.; Ahlrichs, R. Treatment of electronic excitations within the adiabatic approximation of time dependent density functional theory. *Chemical Physics Letters* **1996**, *256*, 454-464.

(73) Bauernschmitt, R.; Ahlrichs, R.; Hennrich, F. H.; Kappes, M. M. Experiment versus time dependent density functional theory prediction of fullerene electronic absorption. *JACS* **1998**, *120*, 5052.

(74) Balasubramani, S. G.; Chen, G. P.; Coriani, S.; Diedenhofen, M.; Frank, M. S.; Franzke, Y. J.; Furche, F.; Grotjahn, R.; Harding, M. E.; Hättig, C.; Hellweg, A.; Helmich-Paris, B.; Holzer, C.; Huniar, U.; Kaupp, M.; Khah, A. M.; Khani, S. K.; Müller, T.; Mack, F.; Nguyen, B. D.; Parker, S. M.; Perlt, E.; Rappoport, D.; Reiter, K.; Roy, S.; Rückert, M.; Schmitz, G.; Sierka, M.; Tapavicza, E.; Tew, D. P.; Wüllen, C. v.; Voora, V. K.; Weigend, F.; Wodynski, A.; Yu, J. M. TURBOMOLE: Modular program suite for ab initio quantum-chemical and condensed-matter simulations. *J. Chem. Phys.* **2020**, *152*, 184107.

(75) Yanai, T.; Tew, D. P.; Handy, N. C. A New Hybrid Exchange-Correlation Functional Using the Coulomb-Attenuating Method (CAM-B3LYP). *Chemical Physics Letters* **2004**, *393*, 51-57.

(76) Perdew, J. P.; Burke, K.; Ernzerhof, M. Generalized Gradient Approximation Made Simple. *Phys. Rev. Lett.* **1996**, *77*, 3865.

(77) Becke, A. D. B3LYP: Density-Functional Thermochemistry III. *Journal of Chemical Physics* **1993**, *98*, 5648-5652.

(78) Stephens, P. J.; Devlin, F. J.; Chabalowski, C. F.; Frisch, M. J. Ab initio Calculation of Vibrational Absorption and Circular Dichroism Spectra Using Density Functional Force Fields. *J. Phys. Chem.* **1994**, *98*, 11623-11627.

(79) Day, P. N.; Nguyen, K. A.; Pachter, R. Calculation of two-photon absorption spectra of donor-acceptor compounds in solution using quadratic response time-dependent density functional theory. *Journal of Chemical Physics* **2006**, *125*, 094103.

(80) Day, P. N.; Nguyen, K. A.; Pachter, R. Calculation of One-Photon and Two-Photon Absorption Spectra of Porphyrins Using Time-Dependent Density Functional Theory. *J. Chem. Theory Comput.* **2008**, *4*, 1094□1106.

(81) Day, P. N.; Nguyen, K. A.; Pachter, R. Calculation of One- and Two-Photon Absorption Spectra of Thiolated Gold Nanoclusters using Time-Dependent Density Functional Theory. *Journal of Chemical Theory and Computation* **2010**, *6*, 2809-2821.

(82) Parker, S. M.; Rappoport, D.; Furche, F. Quadratic Response Properties from TDDFT: Trials and Tribulations. *J. Chem. Theory Comput.* **2018**, *14*, 807−819.

(83) vanderVelden, J. W. A.; Bour, J. J.; Bosman, W. P.; Noordik, J. H. Synthesis and X-Ray Crystal Structure Determination of the Cationic Gold Cluster Compound $[Au_8(PPh_3)_7](NO_3)_2$. *J . Chem. Soc., Chem. Commun.* **1981**, 1218-1219.

(84) Mollenhauer, D.; Gaston, N. Phosphine passivated gold clusters: how charge transfer affects electronic structure and stability. *Phys. Chem. Chem. Phys.* **2016**, *18*, 29686-29697.

(85) Zeng, W.; Gong, S.; Zhong, C.; Yang, C. Prediction of Oscillator Strength and Transition Dipole Moments with the Nuclear Ensemble Approach for Thermally Activated Delayed Fluorescence Emitters. *J. Phys. Chem. C* **2019**, *123*, 10081−10086.

(86) Hammett, L. P. Some Relations between Reaction Rates and Equilibrium Constants. *Chem. Rev.* **1935**, *17*, 125–136.

(87) Lugo, G.; Schwanen, V.; Fresch, B.; Remacle, F. Charge Redistribution Effects on the UV−Vis Spectra of Small Ligated Gold Clusters: a Computational Study. *J. Phys. Chem. C* **2015**, *119*, 10969−10980.

(88) Ceylan, Y. S.; Gieseking, R. L. M. Hydride- and halide-substituted $Au_9(PH_3)_8^{3+}$ nanoclusters: similar absorption spectra disguise distinct geometries and electronic structures. *Phys. Chem. Chem. Phys.* **2021**, *23*, 17287–17299.

(89) Ramesh, G.; Kumar, P. R.; Pillegowda, M.; Periyasamy, G.; Suchetan, P. A.; Butcher, R. J.; Forod, S.; Nagaraju, G. Synthesis, crystal structures, photophysical, electrochemical studies, DFT and TD-DFT calculations and Hirshfeld analysis of new 2,20:60,200-terpyridine ligands with pendant 40-(trimethoxyphenyl) groups and their homoleptic ruthenium complexes. *New J. Chem.* **2020**, *44*, 11471--11489.

(90) Cirri, A.; Silakov, A.; Jensen, L.; Lear, B. J. Probing ligand-induced modulation of metallic states in small gold nanoparticles using conduction electron spin resonance. *Phys. Chem. Chem. Phys.* **2016**, *18*, 25443--25451.

(91) Walter, M.; Akola, J.; Lopez-Acevedo, O.; Jadzinsky, P. D.; Calero, G.; Ackerson, C. J.; Whetten, R. L.; Gronbeck, H.; Hakkinen, H. A unified view of ligand-protected gold clusters as superatom complexes. *Proceedings of National Academy of Science USA* **2008**, *105*, 9157-9162.

(92) Aikens, C. M. Effects of Core Distances, Solvent, Ligand, and Level of Theory on the TDDFT Optical Absorption Spectrum of the Thiolate-Protected Au_{25} Nanoparticle. *J. Phys. Chem. A* **2009**, *113*, 10811.